NASA/CR-1998-206928

Application of Finite Element Method to Analyze Inflatable Waveguide Structures

M. D. Deshpande
ViGYAN, Inc., Hampton, Virginia

February 1998

The NASA STI Program Office ... in Profile

Since its founding, NASA has been dedicated to the advancement of aeronautics and space science. The NASA Scientific and Technical Information (STI) Program Office plays a key part in helping NASA maintain this important role.

The NASA STI Program Office is operated by Langley Research Center, the lead center for NASA's scientific and technical information. The NASA STI Program Office provides access to the NASA STI Database, the largest collection of aeronautical and space science STI in the world. The Program Office is also NASA's institutional mechanism for disseminating the results of its research and development activities. These results are published by NASA in the NASA STI Report Series, which includes the following report types:

- TECHNICAL PUBLICATION. Reports of completed research or a major significant phase of research that present the results of NASA programs and include extensive data or theoretical analysis. Includes compilations of significant scientific and technical data and information deemed to be of continuing reference value. NASA counter-part of peer reviewed formal professional papers, but having less stringent limitations on manuscript length and extent of graphic presentations.
- TECHNICAL MEMORANDUM. Scientific and technical findings that are preliminary or of specialized interest, e.g., quick release reports, working papers, and bibliographies that contain minimal annotation. Does not contain extensive analysis.
- CONTRACTOR REPORT. Scientific and technical findings by NASA-sponsored contractors and grantees.
- CONFERENCE PUBLICATION. Collected papers from scientific and technical conferences, symposia, seminars, or other meetings sponsored or co-sponsored by NASA.
- SPECIAL PUBLICATION. Scientific, technical, or historical information from NASA programs, projects, and missions, often concerned with subjects having substantial public interest.
- TECHNICAL TRANSLATION. English-language translations of foreign scientific and technical material pertinent to NASA's mission.

Specialized services that help round out the STI Program Office's diverse offerings include creating custom thesauri, building customized databases, organizing and publishing research results ... even providing videos.

For more information about the NASA STI Program Office, you can:

- Access the NASA STI Program Home Page at http://www.sti.nasa.gov/STI-homepage.html
- E-mail your question via the Internet to help@sti.nasa.gov
- Fax your question to the NASA Access Help Desk at (301) 621-0134
- Phone the NASA Access Help Desk at (301) 621-0390
- Write to:
  NASA Access Help Desk
  NASA Center for AeroSpace Information
  800 Elkridge Landing Road
  Linthicum Heights, MD 21090-2934

NASA/CR-1998-206928

Application of Finite Element Method to Analyze Inflatable Waveguide Structures

M. D. Deshpande
ViGYAN, Inc., Hampton, Virginia

National Aeronautics and
Space Administration

Langley Research Center
Hampton, Virginia 23681-2199

Prepared for Langley Research Center
under Contract NAS1-19341

February 1998

Available from the following:

NASA Center for AeroSpace Information (CASI)
800 Elkridge Landing Road
Linthicum Heights, MD 21090-2934
(301) 621-0390

National Technical Information Service (NTIS)
5285 Port Royal Road
Springfield, VA 22161-2171
(703) 487-4650

Contents

List of Figures

List of Symbols

a	x-dimension of rectangular waveguide
a_i, b_i, c_i	constants
aa, bb, cc	constants
$\vec{A}$	a vector
A	area of triangular element
b	y-dimension of rectangular waveguide
$\vec{B}$	a vector
$\vec{E}(x, y, z)$	electric field vector
$\vec{E}_t$	transverse electric field vector
E_z	z-component of electric field
e_{tm}	amplitudes of edge basis function
f	scalar function
g_{zn}	amplitude of nodal basis function
G_0	Resonant conductance of shunt slot on a rectangular waveguide
$\vec{H}x, y, z\ )$	magnetic field vector
j	$\sqrt{-1}$
k_0	free-space wave number
k_c	cut off wave number
$\hat{n}$	unit normal vector drawn outwards
$S_{el}(m, m')$	element matrix for single triangular element
$R_{el}(m, m')$	element of coefficient matrix for single triangular element
$Q_{el}(m, m')$	element of coefficient matrix for single triangular element
$P_{el}(m, m')$	element of coefficient matrix for single triangular element
$U_{el}(m, m')$	element of coefficient matrix for single triangular element
$V_{el}(m, m')$	element of coefficient matrix for single triangular element
$X_{el}(m, m')$	element of coefficient matrix for single triangular element
$Y_{el}(m, m')$	element of coefficient matrix for single triangular element
$\vec{T}(x, y, z)$	vector testing function
$\vec{T}_t$	transverse component of testing function

T_z	z-component of testing function
$\overrightarrow{W_{tm}}$	vector basis function associated with triangular element
x, y, z	Cartesian Coordinate system
$\hat{x}, \hat{y}, \hat{z}$	unit vectors along x-, y-, and z-axis, respectively
α_n	scalar basis function associated with a node
ε_0	permittivity of free-space
μ_0	permeability of free-space
ε_r	relative permittivity of medium in region II
μ_r	relative permeability of medium in region II
β	propagation constant
$\beta_{distorted}$	propagation constant for deformed waveguide cross section
$\beta_{undistorted}$	propagation constant for undistorted waveguide cross section
Γ	curve enclosing rectangular cross section
∇_t	$= \left(\hat{x}\frac{\partial}{\partial x} + \hat{y}\frac{\partial}{\partial y}\right)$
θ	Angle of inclination in degrees with respect to x-axis
ϕ	main beam direction in degrees
λ_g	guide wavelength for dominant mode
λ_0	free space wave length

Abstract

A Finite Element Method (FEM) is presented to determine propagation characteristics of deformed inflatable rectangular waveguide. Various deformations that might be present in an inflatable waveguide are analyzed using the FEM. The FEM procedure and the code developed here is so general that it can be used for any other deformations that are not considered in this report. The code is validated by applying the present code to rectangular waveguide without any deformations and comparing the numerical results with earlier published results. The effect of the deformation in an inflatable waveguide on the radiation pattern of linear rectangular slot array is also studied.

1.0 Introduction

Recently there has been considerable interest in the development of inflatable antenna structures [1-3] for space applications. In inflatable antenna technology, the antenna structure is packaged in a small volume during its launch phase and inflated or stretched to its full length after reaching desired orbit. One such structure under development at NASA Langley Research Center is an inflatable slotted rectangular waveguide antenna to be used in soil moisture measuring radiometer. After full deployment of such structure in space, the waveguide surface may have wrinkles, curved walls depending upon the pressure used to inflate the structure, and other unaccounted forces acting on the structure. For successful operation of these antennas, it is desirable to study and estimate adverse effects of these deformations in waveguide walls on the antenna performance. Since these deformations cannot be completely eliminated, study of their effects on antenna performance may lead to determine an allowable level of deformations in these structures reducing high constraint on mechanical design.

An antenna array performance is usually specified by its radiation pattern, input impedance, polarization, etc. For a linear slot array antenna consisting of the shunt slot elements on the broad wall of a rectangular waveguide, the main beam direction is given by [4]

$\cos(\phi) = \left(\pi + \frac{2\pi d}{\lambda_g} + n\pi\right)\lambda_0 / (2\pi d)$ where d is the physical spacing between the elements, λ_g and λ_0 are the guide and free space wavelengths, and $n = 0, \pm 2, \pm 4 ....$ Usually for the broad side radiation at a given frequency of operation the distance d is selected as $\lambda_{g0}/2$, where λ_{g0} is the guide wave length of undistorted waveguide. For $n = -2$, the expression for beam direction becomes $\cos(\phi) = \left(\frac{\lambda_{g0}}{\lambda_g} - 1\right)\lambda_0/\lambda_{g0} = \left(\frac{\beta}{\beta_0} - 1\right)\beta_0/k_0$ where β_0 and β are the dominant mode propagation constants of undistorted and distorted rectangular waveguides, respectively, and k_0 is the free space wave number. From these above expressions it is clear that if $\beta = \beta_0$ then main beam is in the broad side direction. However for β, different from β_0, the main beam shift from the broad side direction as shown in Figure 1. In order to relate various antenna deformations to shift in mean beam direction, it is important to estimate the effects of various deformation in waveguides on the propagation constant β.

In the design of shunt slot array antennas, one of the most important expression designers use is the resonant slot conductance [5] $G_0 = 2.09\left(\frac{k_0}{\beta_0}\frac{a}{b}\right)\left[\cos\left(\frac{\pi}{2}\frac{\beta_0}{k_0}\frac{\beta}{\beta_0}\right)\right]^2\left(\frac{\beta_0}{\beta}\right)$. By selecting proper slot displacement, an amplitude distribution for required radiation pattern is achieved. However for β, different from β_0, which is the case for deformed waveguide, the resonant slot conductance will change and hence the amplitude distribution. Quantitatively the dependance of G_0 on the propagation constant is shown in Figure 2. It is therefore essential to know the propagation constant variation due to deformation in inflatable waveguides.

The purpose of this report is to present an analytical method to determine the electromagnetic fields and propagation constant in a rectangular waveguide with deformed cross sections. A few examples of deformed cross sections that may be present in an inflatable waveguide are shown in Figure 3. The analysis of waveguide with canonical shapes such as rectangular or elliptical (including the circular as a special case) cross section is usually carried out by solving the scalar Helmholtz equation subjected to Dirichlet and Neumann conditions. The electromagnetic field in these cross sections can be written in terms of sine, cosine, or Bessel functions because of the separability of variables[6,7]. However, for the irregular shapes shown in Figure 1, the simple separation of variables method given in [6,7] becomes more tedious and hence not preferred. In this report a versatile and powerful numerical technique, namely the Finite Element Method, is used to analyze these distorted structures.

The problem of finding eigenvalues and propagation constant of a waveguide of an arbitrarily shaped cross section can be solved by invoking the weak form of vector wave equation [8,9]. By dividing the waveguide cross section into triangular subdomains and expressing the electric field (for E-field formulation) or the magnetic field (for H-field formulation) into appropriate vector basis function [9], the weak form of vector wave equation is reduced to a matrix equation. The resulting matrix equation is then solved for eigenvalues and propagation constant using standard mathematical subroutines. The remainder of the report is organized as follows. The formulation of the problem in terms of weak form of vector wave equation and its reduction to a matrix equation is developed in section 2. The detail steps involved in casting the matrix equation into an eigenvalue problem is also given in section 2. The quantitative estimates of effects of waveguide cross section deformation on propagation constant of a L-band rectangular waveguide are given in section 3. The effect of wall distortion on radiation pattern of linear slot arrays on distorted rectangular walls is also numerically studied in section 3. The report is concluded in section 4 with recommendations based on the numerical results presented in section 3 and future work to be completed.

2.0 Theory

2.1 Finite Element E-Field Formulation :

The waveguide cross sections to be analyzed are shown in Figure 3. To determine effects of these irregularities on the cut-off frequency, propagation constant, and characteristic impedance, the numerical technique such as Finite Element Method is developed in this section. The electric field in the cross sections shown in Figure 4 satisfies the Maxwell's equations:

$$\nabla\times\vec{E} = -j\omega\mu\vec{H} \tag{1}$$

$$\nabla\times\vec{H} = j\omega\varepsilon\vec{E} \tag{2}$$

where μ and ε are the permeability and permittivity of the medium. Substituting (1) in (2), the vector wave equation with electric field is obtained as

$$\nabla\times\frac{1}{\mu_r}\left(\nabla\times\vec{E}\right)-k_0^2\varepsilon_r\vec{E} = 0 \tag{3}$$

Similar vector wave equation for the magnetic field can be obtained by substituting (2) in (1). However, we will restrict here to the E-field vector wave equation. Assuming the waveguide to be infinite in the z-direction, the electric field can be written as

$$\vec{E} = \left(\vec{E}_t + \hat{z}E_z\right)e^{-j\beta z} \tag{4}$$

where $\vec{E}_t = \hat{x}E_x + \hat{y}E_y$, $\hat{x}, \hat{y}, \hat{z}$ being the unit vectors along the x-, y-, and z-directions respectively and β is the propagation constant in the z-direction. In the equation (4) it is assumed that the wave is traveling from $z = -\infty$ to $z = +\infty$. Substituting (4) into (3) and carrying out simple mathematical operations, the following equation is obtained:

$$\nabla\times\frac{1}{\mu_r}\left(\nabla\times\vec{E}_t e^{-j\beta z}\right)-k_0^2\varepsilon_r\vec{E}_t e^{-j\beta z}$$

$$+\quad \nabla\times\frac{1}{\mu_r}\left(\nabla\times\hat{z}E_z e^{-j\beta z}\right)-k_0^2\varepsilon_r\hat{z}E_z e^{-j\beta z} = 0 \tag{5}$$

Substituting the gradient operator in equation (5) as $\nabla = \nabla_t - \hat{z}(j\beta)$ and performing simple mathematical manipulation, equation (5) can be written as

$$\nabla_t x\frac{1}{\mu_r}\left(\nabla_t x\vec{E}_t\right)-\frac{1}{\mu_r}\left(j\beta\nabla_t E_z-\beta^2\vec{E}_t\right)-k_0^2\varepsilon_r\vec{E}_t$$

$$-\ \frac{\hat{z}}{\mu_r}\left(\nabla_t\bullet\left(\nabla_t E_z+j\beta\vec{E}_t\right)\right)-k_0^2\varepsilon_r\hat{z}E_z = 0 \tag{6}$$

The equation (6) can be written in component form as

$$\nabla_t x\frac{1}{\mu_r}\left(\nabla_t x\vec{E}_t\right)-\frac{1}{\mu_r}\left(j\beta\nabla_t E_z-\beta^2\vec{E}_t\right)-k_0^2\varepsilon_r\vec{E}_t = 0 \tag{7}$$

$$\frac{1}{\mu_r}\left(\nabla_t\bullet\left(\nabla_t E_z+j\beta\vec{E}_t\right)\right)+k_0^2\varepsilon_r E_z = 0 \tag{8}$$

In order to make coefficients of field components real, equations (7) and (8) after the substitution $E_z = j\beta E_z$ are written as

$$\nabla_t x\frac{1}{\mu_r}\left(\nabla_t x\vec{E}_t\right)+\frac{\beta^2}{\mu_r}\left(\nabla_t E_z+\vec{E}_t\right)-k_0^2\varepsilon_r\vec{E}_t = 0 \tag{9}$$

$$\frac{1}{\mu_r}\left(\nabla_t\bullet\left(\nabla_t E_z+\vec{E}_t\right)\right)+k_0^2\varepsilon_r E_z = 0 \tag{10}$$

The expressions (9) and (10) are required equations to be solved either for the propagation constant β for a given frequency or for the cut-off wave number $k_c = k_0$ for $\beta = 0$. In either case to solve equations (9) and (10) using the Galerkin's procedure, we select a testing function $\vec{T} = \vec{T}_t + \hat{z}T_z$. Multiply equations (9) and (10) with $\vec{T}_t$ and T_z, respectively, and integrating over the cross section we get

$$\int_{cross-section}\int \left(\nabla_t x \frac{1}{\mu_r}\left(\nabla_t x \vec{E}_t \right) + \frac{\beta^2}{\mu_r}\left(\nabla_t E_z + \vec{E}_t \right) - k_0^2 \varepsilon_r \vec{E}_t \right) \bullet \vec{T}_t dxdy = 0 \tag{11}$$

$$\int_{cross-section}\int \left(\frac{1}{\mu_r}\nabla_t \bullet \left(\nabla_t E_z + \vec{E}_t \right) + k_0^2 \varepsilon_r E_z \right) T_z dxdy = 0 \tag{12}$$

Using the vector identities

$$\vec{A} \bullet \nabla_t x \vec{B} = \nabla_t x \vec{A}_t \bullet \vec{B} - \nabla_t \bullet \left(\vec{A} \times \vec{B} \right)$$

$$\int_{cross-section}\int \left(\nabla_t \bullet \left(\vec{A} \times \vec{B} \right) \right) dxdy = \int_{\Gamma} \left(\vec{A} \times \vec{B} \right) \bullet \hat{n} dl = -\int_{\Gamma} \left(\hat{n} \times \vec{B} \right) \bullet \vec{A} dl$$

$$f \nabla_t \bullet \vec{A} = + \nabla_t \bullet f \vec{A} - \vec{A} \bullet \nabla_t f$$

$$\int_{cross-section}\int \nabla_t \bullet \vec{A} \; dxdy = \int_{\Gamma} \vec{A} \bullet \hat{n} dl$$

where $\hat{n}$ is the outward drawn unit normal vector to the curve Γ enclosing the cross section.

equations (11) and (12) can be written as

$$\int_{cross-section}\int \left(\nabla_t x \vec{T}_t \bullet \frac{1}{\mu_r} \nabla_t x \vec{E}_t - \left(k_0^2 \varepsilon_r - \frac{\beta^2}{\mu_r} \right) \left(\vec{E}_t \bullet \vec{T}_t \right) \right) dxdy$$

$$+ \int_{cross-section}\int \frac{\beta^2}{\mu_r} \nabla_t E_z \bullet \vec{T}_t dxdy = -\int_{\Gamma} \vec{T}_t \bullet \hat{n} \times \frac{1}{\mu_r} \nabla_t x \vec{E}_t d\Gamma \tag{13}$$

and

$$\int_{cross-section}\int \left(\nabla_t T_z \bullet \frac{1}{\mu_r} \nabla_t E_z - k_0^2 \varepsilon_r E_z T_z \right) dxdy + \int_{cross-section}\int \nabla_t T_z \bullet \frac{1}{\mu_r} \vec{E}_t \; dxdy$$

$$= \int_{\Gamma} \frac{1}{\mu_r} T_z \nabla_t E_z \bullet \hat{n} d\Gamma + \int_{\Gamma} \frac{1}{\mu_r} T_z \vec{E}_t \bullet \hat{n} d\Gamma \tag{14}$$

where $\hat{n}$ is the outward drawn unit normal vector to the curve Γ enclosing the cross section. To solve the weak forms of differential equations given in (13) and (14) numerically, the cross section shown in Figure 4(a) is discretized into triangular domain as shown in figure 4(b). The transverse and longitudinal components over a triangle (shown in 5) are then expressed as

$$\vec{E}_t = \sum_{m=1}^{3} e_{tm}\vec{W}_{tm}(x, y) \tag{15}$$

$$E_z = \sum_{n=1}^{3} g_{zn}\alpha_n(x, y) \tag{16}$$

where m =1,2,3 are the three edges of the triangle and n = 1,2,3 are the three nodes of the triangle.

The detail derivation of the vector edge basis function $\vec{W}_{tm}$ and the scalar basis function $\alpha_n(x, y)$ are given in Appendix A. Substituting (15) and (16) in (13) and (14) we get

$$\sum_{m=1}^{3} e_{tm} \int_{triangle}\int\left(\nabla_t x\vec{W}_{tm'} \bullet \frac{1}{\mu_r}\nabla_t x\vec{W}_{tm} - k_0^2\varepsilon_r\left(\vec{W}_{tm} \bullet \vec{W}_{tm'}\right)\right)dxdy$$

$$+ \frac{\beta^2}{\mu_r}\left(\sum_{n=1}^{3} g_{zn} \int_{triangle}\int\nabla_t\alpha_n \bullet \vec{W}_{tm'}dxdy + \sum_{m=1}^{3} e_{tm} \int_{triangle}\int\vec{W}_{tm} \bullet \vec{W}_{tm'}dxdy\right)$$

$$= -\int_{\Gamma}\vec{T}_t \bullet \hat{n} \times \frac{1}{\mu_r}\nabla_t x\vec{E}_t d\Gamma \tag{17}$$

$$\sum_{m=1}^{3} e_{tm} \int_{triangle}\int\nabla_t\alpha_{n'} \bullet \vec{W}_{tm}dxdy + \sum_{n=1}^{3} g_{zn} \int_{triangle}\int\left(\nabla_t\alpha_{n'} \bullet \frac{1}{\mu_r}\nabla_t\alpha_n - k_0^2\varepsilon_r(\alpha_n\alpha_{n'})\right)dxdy$$

$$= + \sum_{n=1}^{3} g_{zn}\int_{\Gamma}\frac{1}{\mu_r}\alpha_{n'}\nabla_t\alpha_n \bullet \hat{n}d\Gamma + \sum_{m=1}^{3} e_{tm}\int_{\Gamma}\frac{1}{\mu_r}\alpha_{n'}\vec{W}_{tm} \bullet \hat{n}d\Gamma \tag{18}$$

For the waveguide cross section enclosed by metallic boundaries, the line integrals appearing on right hand sides of equations (17) and (18) are always zero. This is true because of the tangential electric field being zero on the perfectly conducting boundaries. With these considerations, the equations (17) and (18) can be written in a matrix form

$$\begin{bmatrix} S_{el}(m', m) & 0 \\ 0 & 0 \end{bmatrix}\begin{bmatrix} e_{tm} \\ g_{zn} \end{bmatrix} = -\beta^2\begin{bmatrix} R_{el}(m', m) & Q_{el}(m', n) \\ Q_{el}(n', m) & P_{el}(n', n) \end{bmatrix}\begin{bmatrix} e_{tm} \\ g_{zn} \end{bmatrix} \tag{19}$$

suitable for calculations of propagation constant for a given frequency.

For calculation of cut-off wave number when $\beta = 0$ the equation (17) and (18) can be written in a matrix form

$$\begin{bmatrix} U_{el}(m', m) & 0 \\ 0 & V_{el}(n', n) \end{bmatrix} \begin{bmatrix} e_{tm} \\ g_{zn} \end{bmatrix} = k_c^2 \begin{bmatrix} X_{el}(m', m) & 0 \\ 0 & Y_{el}(n', n) \end{bmatrix} \begin{bmatrix} e_{tm} \\ g_{zn} \end{bmatrix} \tag{20}$$

suitable for calculation of cut-off wave number. The elements of various submatrices appearing in equations (19) and (20) are given by

$$S_{el}(m', m) = \int_{triangle}\int \left(\nabla_t x \vec{W}_{tm'} \bullet \frac{1}{\mu_r} \nabla_t x \vec{W}_{tm} - k_0^2 \varepsilon_r \left(\vec{W}_{tm} \bullet \vec{W}_{tm'} \right) \right) dxdy \tag{21}$$

$$R_{el}(m', m) = \frac{1}{\mu_r} \int_{triangle}\int \vec{W}_{tm} \bullet \vec{W}_{tm'} dxdy \tag{22}$$

$$Q_{el}(m', n) = \frac{1}{\mu_r} \int_{triangle}\int \nabla_t \alpha_n \bullet \vec{W}_{tm'} dxdy \tag{23}$$

$$P_{el}(n', n) = \int_{triangle}\int \left(\nabla_t \alpha_{n'} \bullet \frac{1}{\mu_r} \nabla_t \alpha_n - k_0^2 \varepsilon_r (\alpha_n \alpha_{n'}) \right) dxdy \tag{24}$$

$$U_{el}(m', m) = \int_{triangle}\int \left(\nabla_t x \vec{W}_{tm'} \bullet \frac{1}{\mu_r} \nabla_t x \vec{W}_{tm} \right) dxdy \tag{25}$$

$$V_{el}(n', n) = \int_{triangle}\int \left(\nabla_t \alpha_{n'} \bullet \frac{1}{\mu_r} \nabla_t \alpha_n \right) dxdy \tag{26}$$

$$X_{el}(m', m) = \int_{triangle}\int \varepsilon_r \left(\vec{W}_{tm} \bullet \vec{W}_{tm'} \right) dxdy \tag{27}$$

$$Y_{el}(n', n) = \int_{triangle}\int \varepsilon_r \alpha_n \alpha_{n'} dxdy \tag{28}$$

The double integrations over the triangle appearing in (21)-(28) are numerically evaluated. Details of the numerical integration are given in Appendix B.

3.0 Numerical Results

A FORTRAN code is written to solve the eigenvalue problems described in equations (19) and (20). The matrix elements appearing in (19) and (20) are evaluated numerically (see Appendix B). To validate the code, the cutoff wave numbers for various modes in a rectangular waveguide without wall distortion are first determined and compared with analytical results [7].

3.1 Rectangular Waveguide Without Wall Distortion:

The eigenvalues are then determined using standard mathematical subroutines. For validation of the code, a rectangular waveguide with $\frac{a}{b} = 2$ and without wall distortion is selected as a first example. The cut-off wave numbers calculated using the present code are given in Table 1 along with the results reported earlier [7]. It is found that the percentage error in the calculated wave numbers using the present code is very small (less than 3 percent). From the results shown in Table 1, it is also observed that the percentage error increases with the mode order.

Table 1: Cut-off wave number of rectangular waveguide a/b =2

Modes	$k_c a$		
	Reference [1]	Present Method	%Error
		TE Modes	
TE_{10}	3.142	3.1397	0.007
TE_{20}	6.285	6.276	0.143
TE_{01}	6.285	6.267	0.286
TE_{11}	7.027	7.139	1.59
TE_{30}	9.428	9.376	0.552
TE_{21}	8.889	9.115	2.54
		TM Modes	
TM_{11}	7.027	7.026	0.001
TM_{21}	8.889	8.9012	0.137
TM_{31}	11.331	11.337	0.052

For the second example, an inhomogenuos rectangular waveguide without any wall distortion as shown in Figure 6 is considered. For this geometry, using the present code the propagation constant as a function of frequency is calculated and given in Table 2 along with earlier published data. The numerical results obtained by the present code are within 5 percent of the analytical results [7,9].

Table 2: Dispersion characteristic of lowest order in a rectangular waveguide

b/λ	β/k_0 For lowest order mode		
	Reference [1}	Present Method	% Error
0.2	0.48	0.462	3.75
0.3	1.00	1.01	1.00
0.4	1.18	1.18	0.00
0.5	1.26	1.28	1.59
0.6	1.30	1.36	4.62

3.2 Rectangular waveguide with wall distortion:

In an inflatable rectangular waveguide, distortion in the walls may be of type shown in Figure 3. In this section, effect of each type of distortion on the propagation constant is numerically studied. It should be noted that while analyzing the effects of distortion, the perimeter of distorted waveguide remains the same as that of undistorted waveguide. This is due to inelastic characteristics of the material used for the inflatable waveguide. In the present code, under the constant perimeter constrain effect of each type of distortion, the propagation constant is numerically studied.

3.2.1 Inclined walls in y-direction:

A rectangular waveguide with inclined walls in y-direction is shown in Figure 7. The dispersion characteristics $\beta_{distorted}$ of an L-band rectangular waveguide with dimension $16.5\ x\ 8.26$ cm and walls in the y-direction inclined at θ are calculated using the present code. If $\beta_{undistorted}$ is the dispersion characteristics of undistorted L band rectangular waveguide, the percentage change in the dispersion characteristics of distorted waveguide is given by

$$\text{percentage Change in } \beta = \frac{\beta_{distorted} - \beta_{undistorted}}{\beta_{undistorted}} 100 \tag{29}$$

The percentage change in the dispersion characteristics using (29) is then calculated and presented in Figure 8 for various values of θ. From Figure 8 it may be concluded that there is not a significant effect of the distortion shown in Figure 7 on the propagation characteristics. Figure 9 shows the electric field pattern in the cross section of the rectangular waveguide. The arrow direction gives the direction of electric field and the length of arrows show the magnitude of the electric field.

3.2.2 Inclined walls in x-direction:

A rectangular waveguide with inclined walls in the x-direction is shown in Figure 10. The dispersion characteristics $\beta_{distorted}$ of an L-band rectangular waveguide with dimension $16.5\ x\ 8.26$ cm and walls in the x-direction inclined at θ are calculated using the present code. The percentage change in the dispersion characteristics using (29) is then calculated and presented in Figure 11 for various values of θ. Figure 12 shows the electric field pattern in the cross section of the rectangular waveguide. The arrow direction gives the direction of electric field and the length of arrows shows the magnitude of the electric field.

3.2.3 Rectangular waveguide with curved walls:

Rectangular waveguides with curved walls may take shapes as shown in Figures 13, 16, 19, 22, 25, and 28. These waveguide shapes are modelled using GEOSTAR, and the percentage change in the dispersion characteristics calculated using equation (29) is presented in Figures 14, 17, 20, 23, 26, and 29. Corresponding electric field plots for these geometries are shown in Figures 15, 18, 21, 24, 27, and 30. From Figures 14, 17, and 20 it may be concluded that distortions of forms given in Figures 16 and 19 cause more changes in propagation constant than the distortion shown in Figure 13. Similar conclusion may be drawn from Figures 23, 26, and 29. The distortion of forms given in Figures 25 and 28 cause more changes in the propagation constant than the distortion shown in Figure 23.

3.2.4 Rectangular waveguide with randomly distorted walls:

A rectangular waveguide with distorted walls is shown in Figure 31. The randomly distorted rectangular cross section shown in Figure 31 is obtained using the following procedure. Random distortion in the walls is obtained by using a random number satisfying Gaussian distribution with varience $\sigma^2 = 0.2$ and zero mean value. Using the tolerance of ± 0.2 and variance $\sigma^2 = 0.2$, random numbers satisfying the Gaussian distribution are generated. A randomly distorted cross section of L-band rectangular waveguide as shown in Figure 31 is then obtained by displacing the boundary nodes of undistorted L-band rectangular waveguide using these random numbers. The percentage change in the dispersion characteristics using (29) is then calculated for $\sigma^2 = 0.2$ for the tolerance of 0.2. In order to determine the true statistical nature, 50 runs were performed for $\sigma^2 = 0.2$ and tolerance equal to 0.2 and the percentage change in the dispersion characteristics for each case are presented in Figure 32. From these results, mean and standard deviation values for the β are calculated and presented in Figure 33. Figures 34 and 35 show results of similar run for $\sigma^2 = 0.2$ and the tolerance equal to ± 0.1.

4.0 Conclusion

Simple formulas are developed to show dependence of slot array performance on the dominant mode propagation constant of the rectangular waveguide feeding the slot array. Using the Finite Element Method it has been shown how various types of mechanical deformation can alter the propagation constant and hence the array performance. The variety of deformation/ distortions that might be present in an inflatable rectangular waveguide are analyzed and their effects on the dominant mode propagation constant are numerically studied. The study will help in determining allowable dimensional tolerances in an inflatable rectangular waveguide to be used in the space antennas.

Appendix A

A.1 Derivation of Nodal Basis Function:

Consider a triangle as shown in Figure 5 where e_{z1}, e_{z2}, e_{z3} are the amplitudes of z-component of electric field at the three nodes reduplicative. Assuming linear variation over the triangle, $E_z(x, y)$ can be written as

$$E_z(x, y) = aa + bbx + ccy \tag{30}$$

The constants aa, bb, cc can be determined from

$$\begin{bmatrix} aa \\ bb \\ cc \end{bmatrix} = \begin{bmatrix} 1 & x_1 & y_1 \\ 1 & x_2 & y_2 \\ 1 & x_3 & y_3 \end{bmatrix}^{-1} \begin{bmatrix} e_{z1} \\ e_{z2} \\ e \end{bmatrix} \tag{31}$$

Substituting (31) into (30) and rearranging the terms, (30) can be written as

$$E_z(x, y) = \sum_{i=1}^{3} e_{zi}\alpha_i(x, y) \tag{32}$$

where

$$\alpha_i(x, y) = \frac{1}{2A}(a_i + b_i x + c_i y) \text{ with } i = 1, 2, 3 \tag{33}$$

$$a_i = x_j y_k - x_k y_j \tag{34}$$

$$b_i = y_j - y_k \tag{35}$$

$$c_i = x_k - x_j \tag{36}$$

$$A = \frac{1}{2}\begin{vmatrix} 1 & x_1 & y_1 \\ 1 & x_2 & y_2 \\ 1 & x_3 & y_3 \end{vmatrix} \tag{37}$$

$\alpha_i(x, y)$ given in (33) is the required nodal basis function.

A.2 Derivation of Vector Edge Basis Function:

From the current basis functions given in [10] the vector edge function for the edge between nodes 2 and 3 (see 5) can be written as

$$\vec{W}_1 = \frac{L_1}{2A}\hat{z} \times (\hat{x}(x - x_1) + \hat{y}(y - y_1)) \tag{38}$$

The vector edge function defined in (38) satisfies the condition $\nabla_t \bullet \vec{W}_1 = 0$; and if $\hat{t}_1$ is the unit vector along the #1 edge, then $\hat{t}_1 \bullet \vec{W}_1 = 1$. The edge vector functions in general can be written as

$$\vec{W}_i = \frac{L_i}{2A}\hat{z} \times (\hat{x}(x - x_i) + \hat{y}(y - y_i)) \tag{39}$$

$\vec{W}_i$ given in (39) is the required vector edge basis function.

Appendix B

B.1 Expressions for Matrix Elements:

Using the basis function given in (33) and (39) and using expressions (21)-(28), the matrix elements of matrix equations (19) and (20) can be written as

$$S_{el}(m', m) = \frac{1}{\mu_r}\frac{L_m L_{m'}}{A} - \frac{k_0^2\varepsilon_r}{4A^2}\int_{triangle}\int((x-x_m)(x-x_{m'}) + (y-y_m)(y-y_{m'}))\,dxdy \quad (40)$$

$$R_{el}(m', m) = \frac{1}{\mu_r 4A^2}\int_{triangle}\int((x-x_m)(x-x_{m'}) + (y-y_m)(y-y_{m'}))\,dxdy \quad (41)$$

$$Q_{el}(m', i) = \frac{1}{\mu_r 4A^2}\int_{triangle}\int(c_i(x-x_{m'}) - b_i(y-y_{m'}))\,dxdy \quad (42)$$

$$P_{el}(i', i) = \left(\frac{1}{\mu_r 4A}(b_{i'}b_i + c_i c_{i'}) - \frac{k_0^2\varepsilon_r}{4A^2}\int_{triangle}\int(a_i + b_i x + c_i y)(a_{i'} + b_{i'}x + c_{i'}y))\,dxdy\right) \quad (43)$$

$$U_{el}(m', m) = \frac{1}{\mu_r}\frac{L_m L_{m'}}{A} \quad (44)$$

$$V_{el}(i', i) = \frac{1}{\mu_r 4A}(b_{i'}b_i + c_i c_{i'}) \quad (45)$$

$$X_{el}(m', m) = \frac{\varepsilon_r}{4A^2}\int_{triangle}\int((x-x_m)(x-x_{m'}) + (y-y_m)(y-y_{m'}))\,dxdy \quad (46)$$

$$Y_{el}(i', i) = \frac{\varepsilon_r}{4A^2}\int_{triangle}\int(a_i + b_i x + c_i y)(a_{i'} + b_{i'}x + c_{i'}y))\,dxdy \quad (47)$$

Using 13 point integration formulas given in [11], the integration over triangle appearing in (40)-(47) are evaluated.

References

[1] R. Freeland, et al., “Inflatable antenna technology with preliminary shuttle experiment results and potential applications, ” Eighteenth Annual Meeting & Symposium Antenna Measurement Techniques Association, pp. 3-8, Sept. 30-Oct. 3, 1996, Seattle, Washington.

[2] R. E. Freeland, et al., “ Development of flight hardware for large, inflatable-deployable antenna experiment, ” IAF Paper 95-1.5.01, presented at the 46th Congress of the International Astronautical Federation, Oslo, Norway, October 2-6, 1995.

[3] R. E. Freeland, et al., " Validation of a unique concept for a low-cost, light weight space-deployable antenna structure, " IAF Paper 93-I.1.204, Presented at the 44th Congress of the International Astronautical Federation, Graz, Austria, October 16, 1993.

[4] R. S. Elliott, "*Antenna Theory and Design*, " Prentice Hall, Inc., 1981.

[5] H. Jasik, " *Antenna Engineering Handbook*, " McGraw-Hill Book Co., Inc., 1961.

[6] R. E. Collins, "*Field Theory of Guided Waves*, " McGraw Hill Book Company, 1961.

[7] R. F. Harrington, "*Time-Harmonic Electromagnetic Field*, " McGraw-Hill Book Co., Inc., 1961.

[8] J. Jin, "*The finite element method in electromagnetics*, " John Wiley & Sons, Inc., New York, 1993.

[9] C. J. Reddy, et al., "Finite element method for eigenvalue problem in electromagnetics, " NASA Technical Paper 3485, December 1994.

[10] S. M. Rao, D. R. Wilton, and A. W. Glisson, "Electromagnetic scattering by surfaces of arbitrary shape, " IEEE Trans. on Antennas and Propagation, Vol. AP-30, pp. 409-418, March 1982.

[11] J. N. Reddy, "*An introduction to the finite element method*, " McGraw-Hill Book Company, 1984.

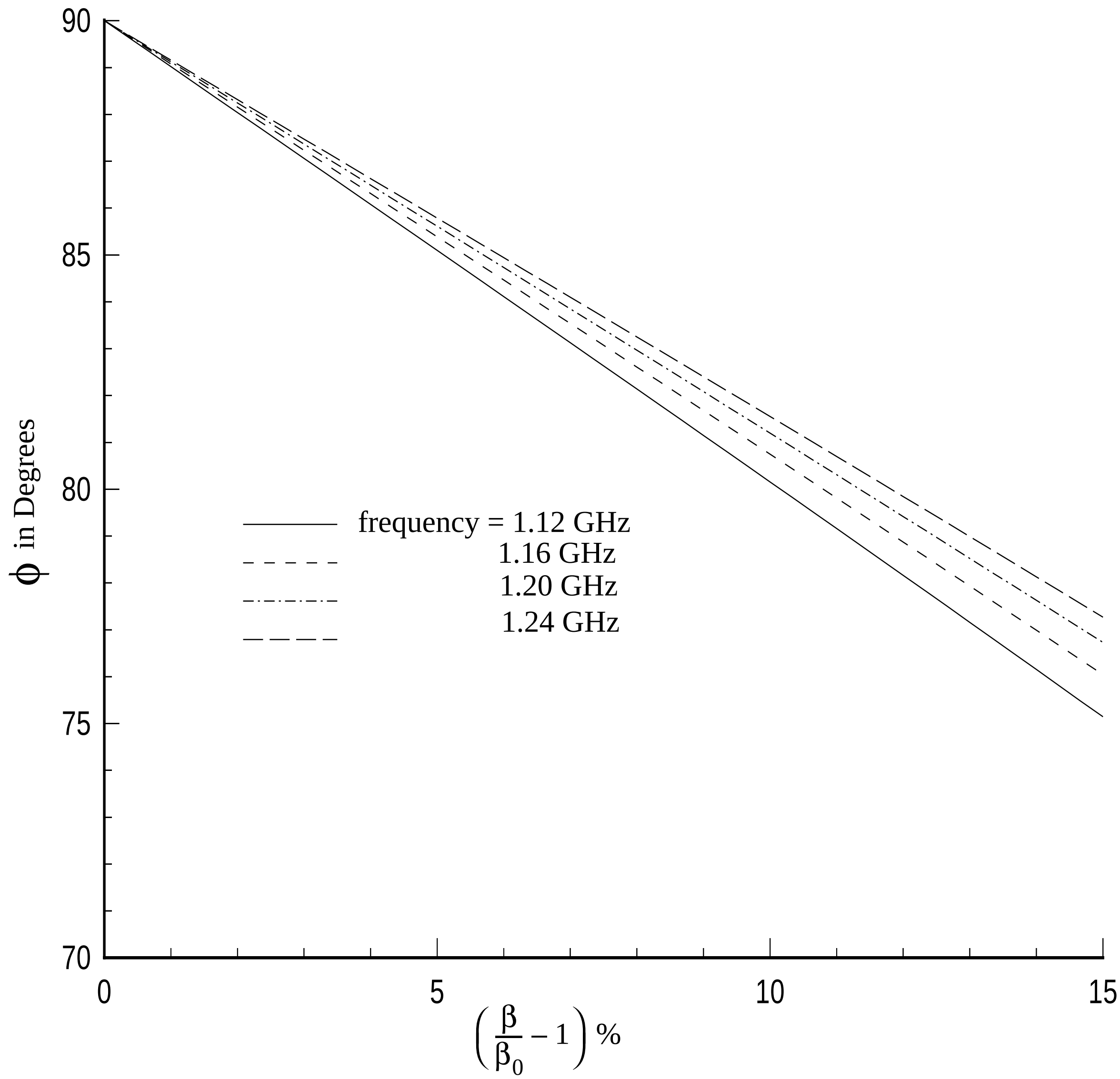

Figure 1 Plot of main beam direction ϕ as function of $\frac{\beta}{\beta_0}$.

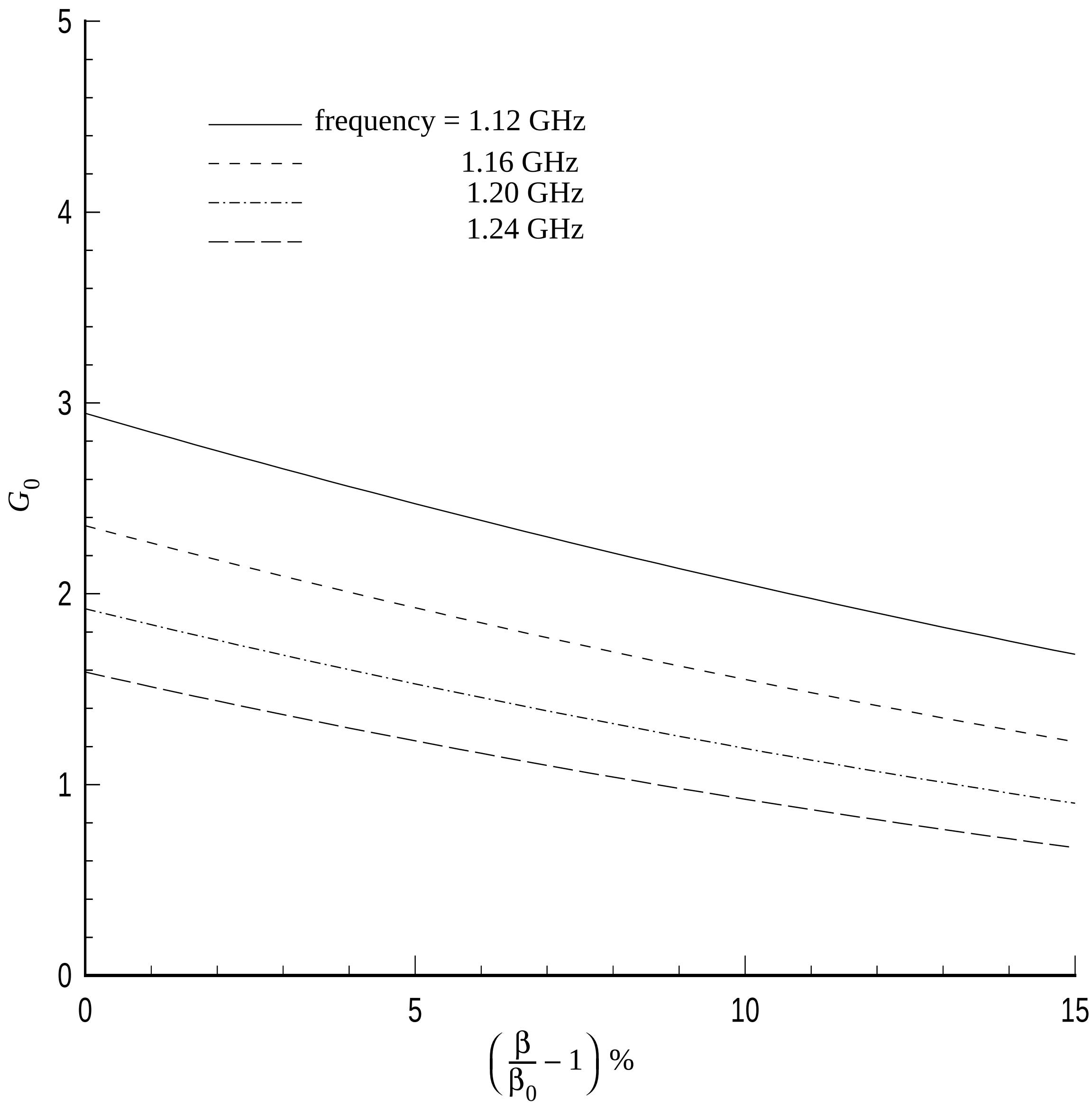

Figure 2 Plot of resonant slot conductance G_0 as a function of $\frac{\beta}{\beta_0}$.

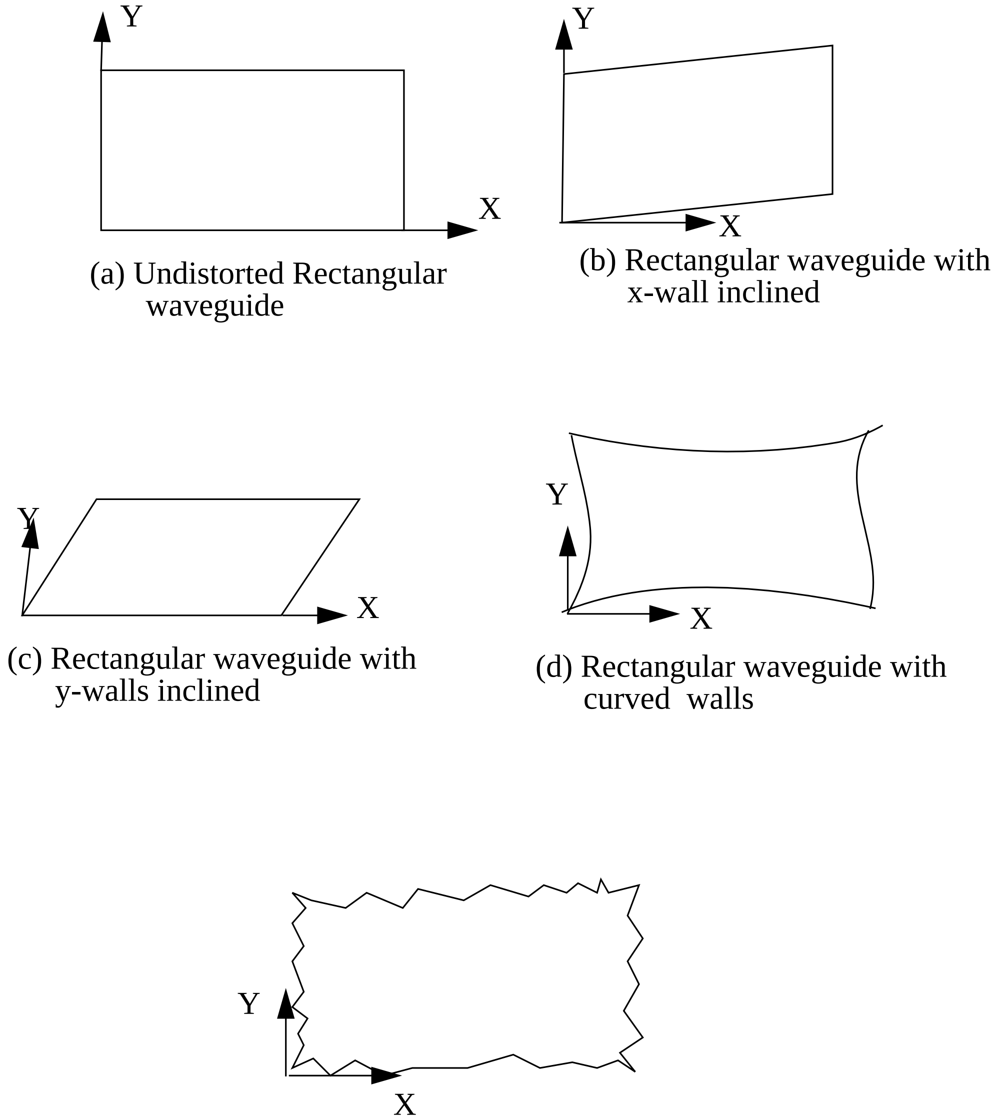

(a) Undistorted Rectangular waveguide

(b) Rectangular waveguide with x-wall inclined

(c) Rectangular waveguide with y-walls inclined

(d) Rectangular waveguide with curved walls

(e) Rectangular waveguide with wrinkles in walls

Figure 3 Geometry of few cross sections of deformed rectangular waveguide.

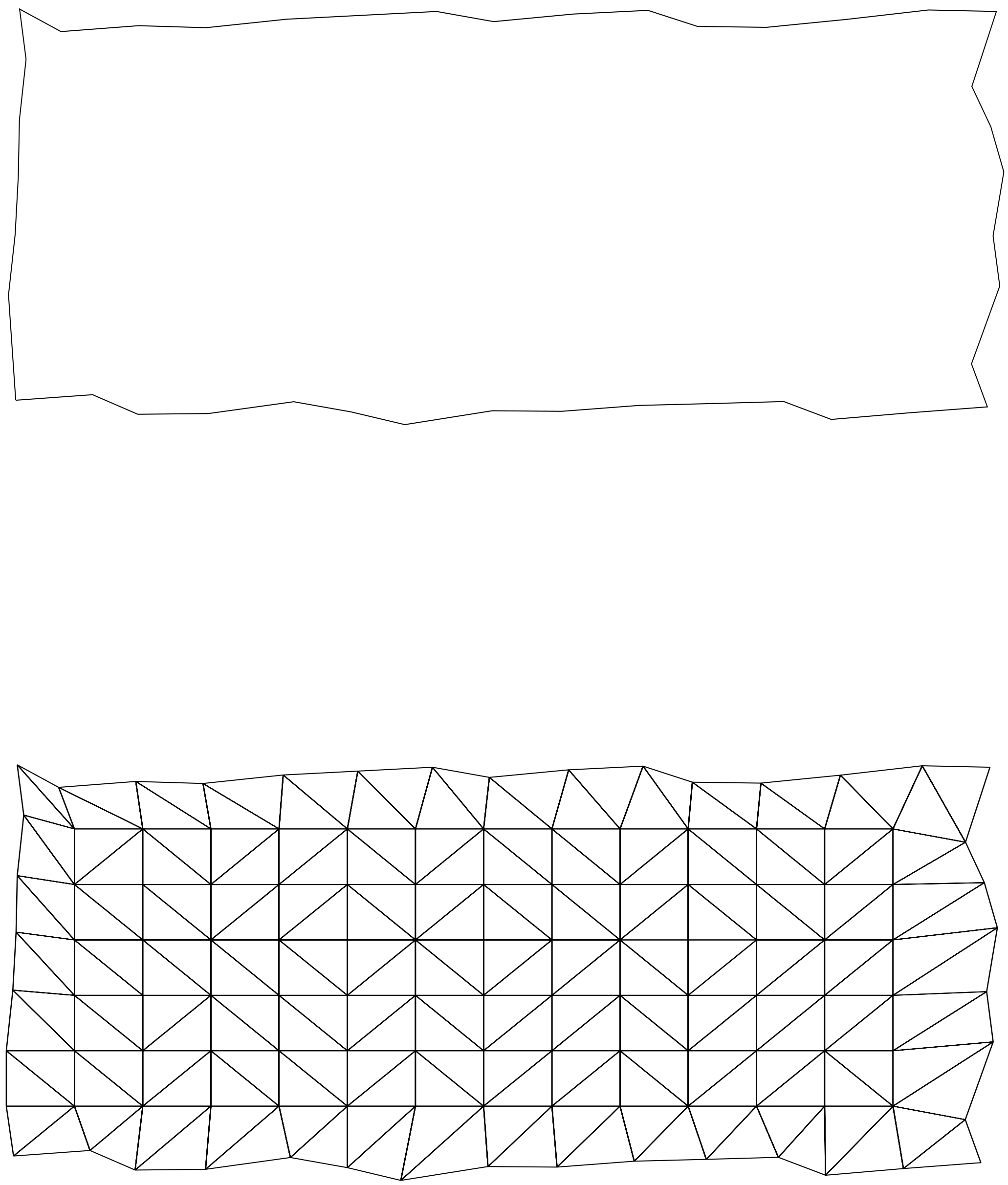

Figure 4 Geometry of cross section of a rectangular waveguide with distorted walls.

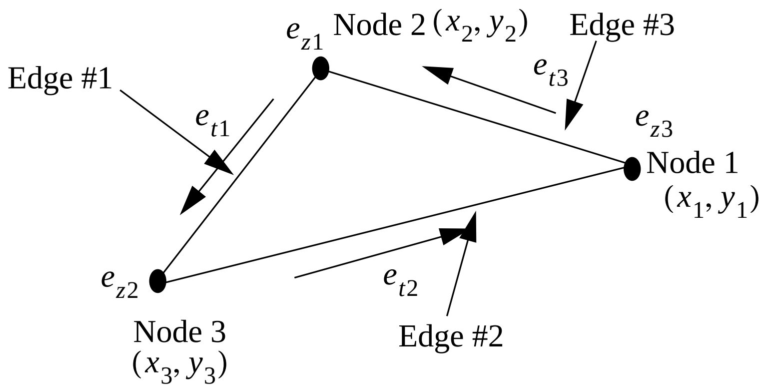

Figure 5 Geometry of a triangular element.

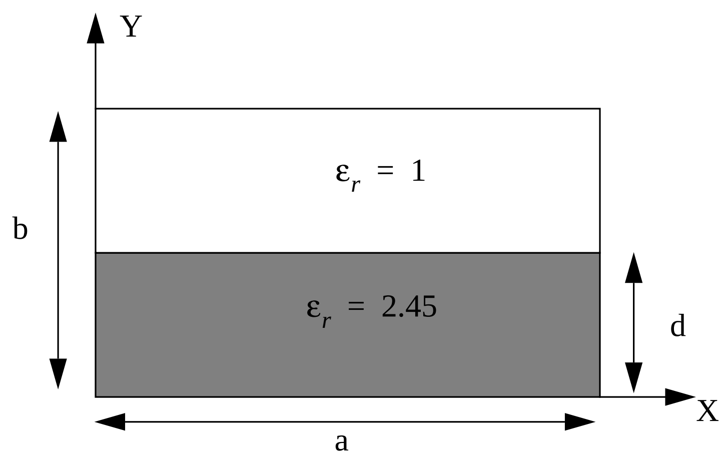

Figure 6 Geometry of inhomogeneous rectangular waveguide with $\frac{b}{a} = 0.45$ and $\frac{d}{b} = 0.5$.

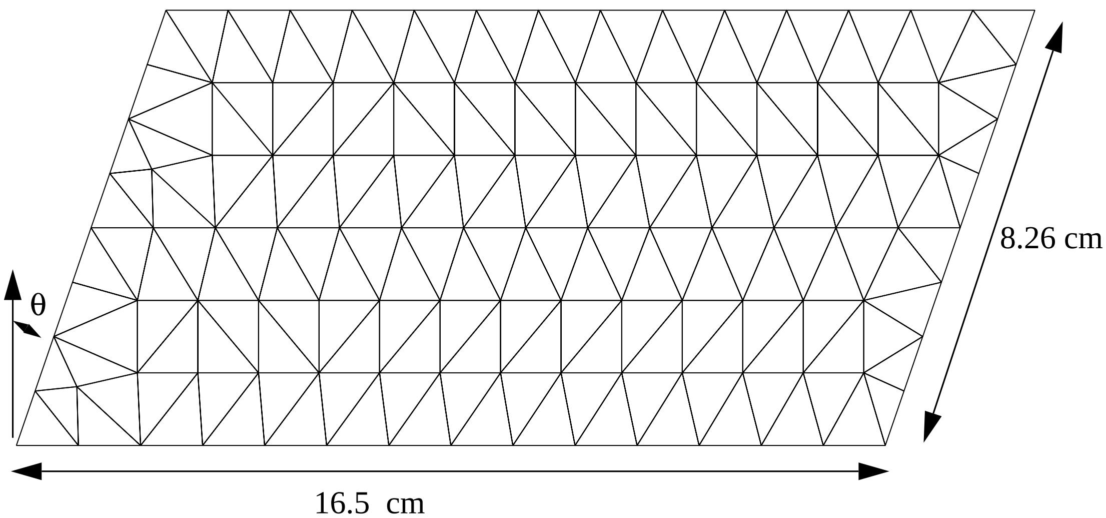

Figure 7 Geometry of L-band rectangular waveguide with inclined walls in y-direction.

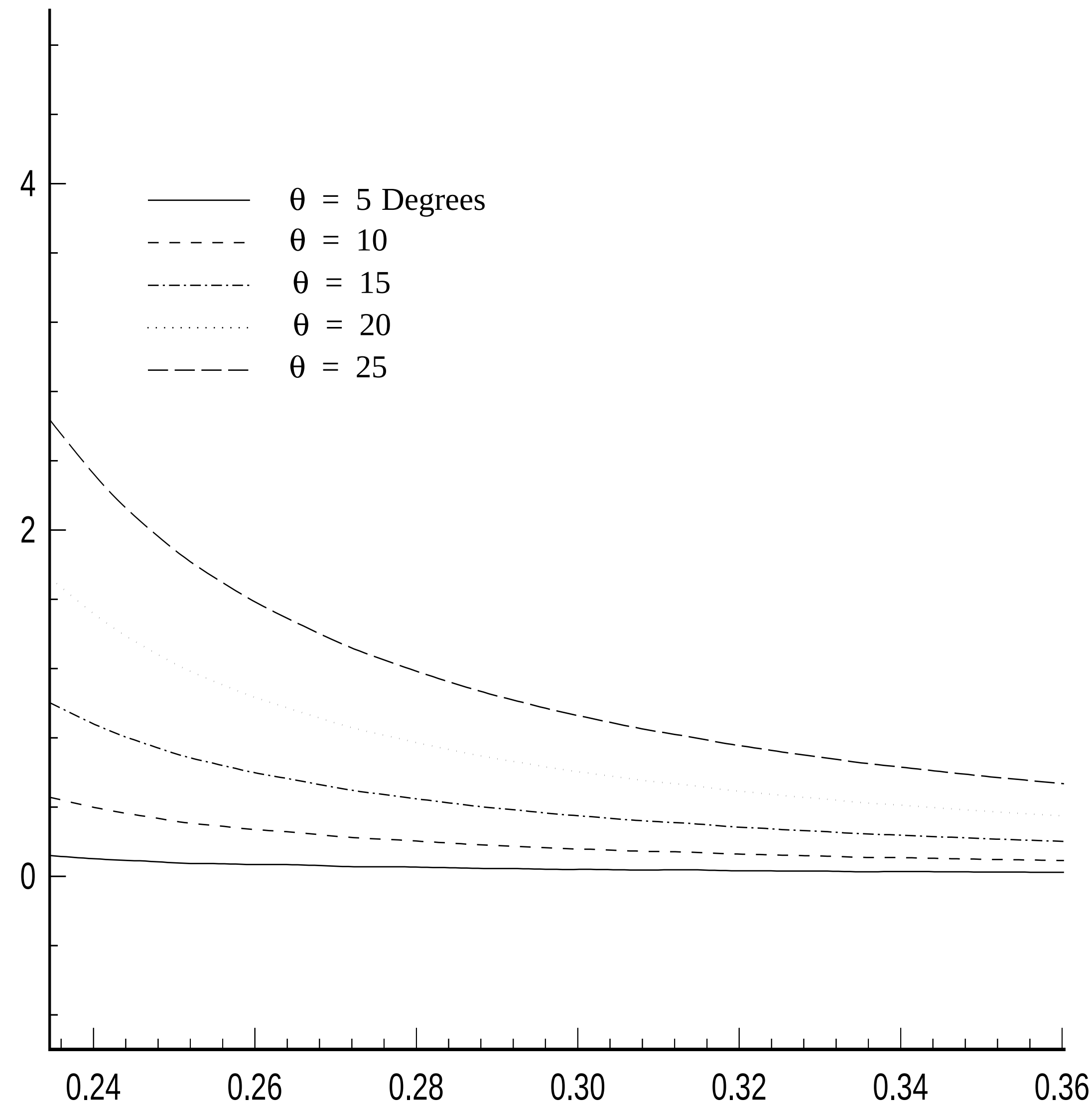

Figure 8 Plot of percentage change in dispersion characteristics of L-band rectangular waveguide for various inclination, θ , in y-direction.

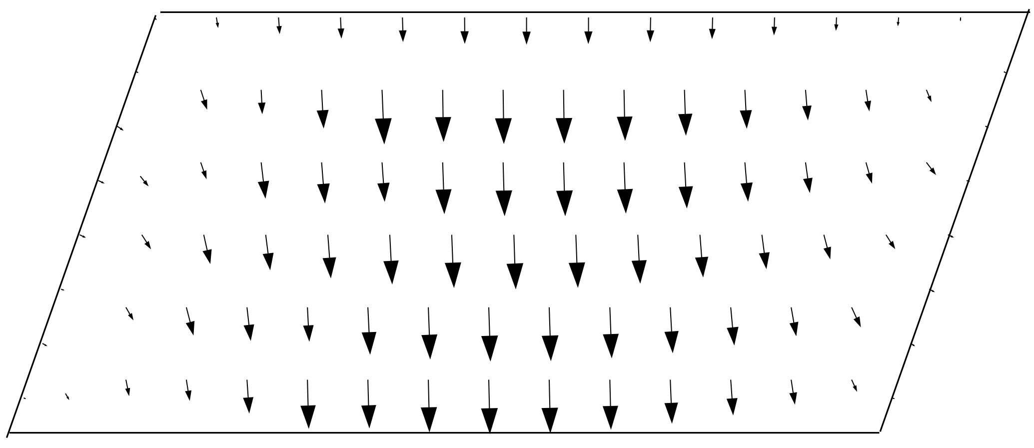

Figure 9 Electric field in the cross section of distorted L-band rectangular waveguide shown in Figure 7.

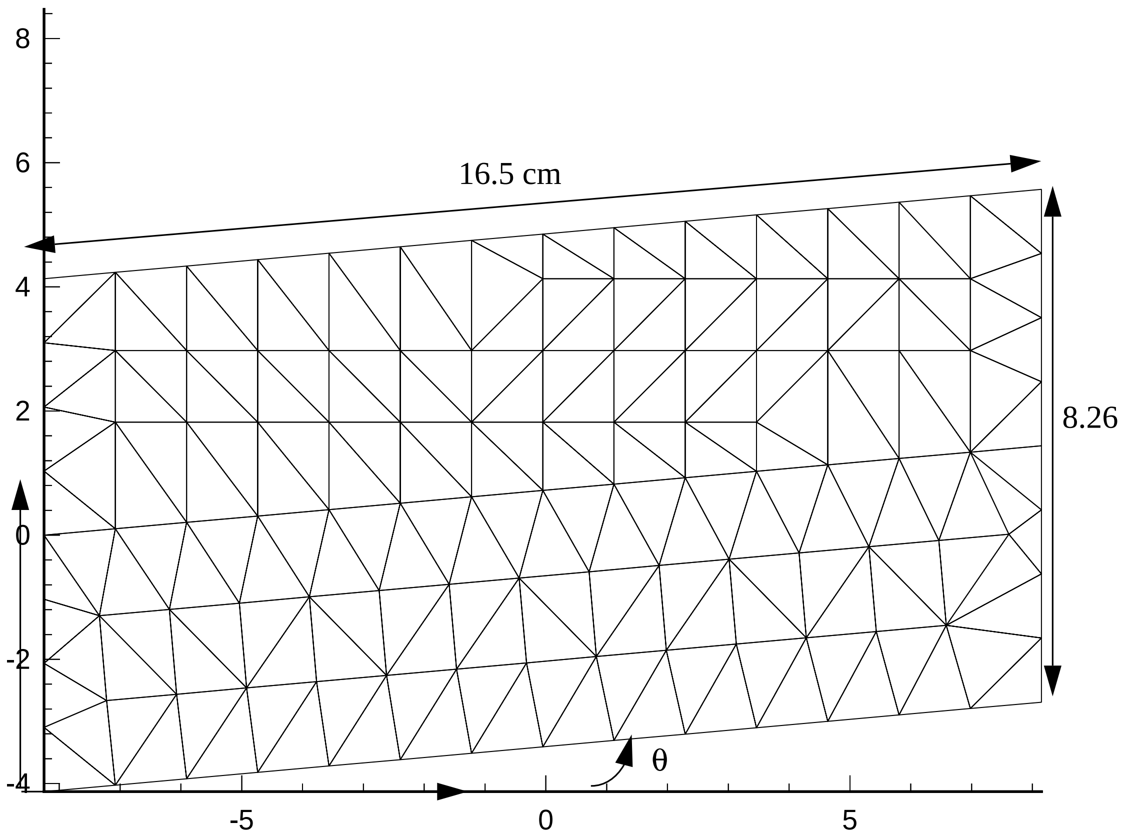

Figure 10 Geometry of L-band rectangular waveguide with inclined walls in x-direction.

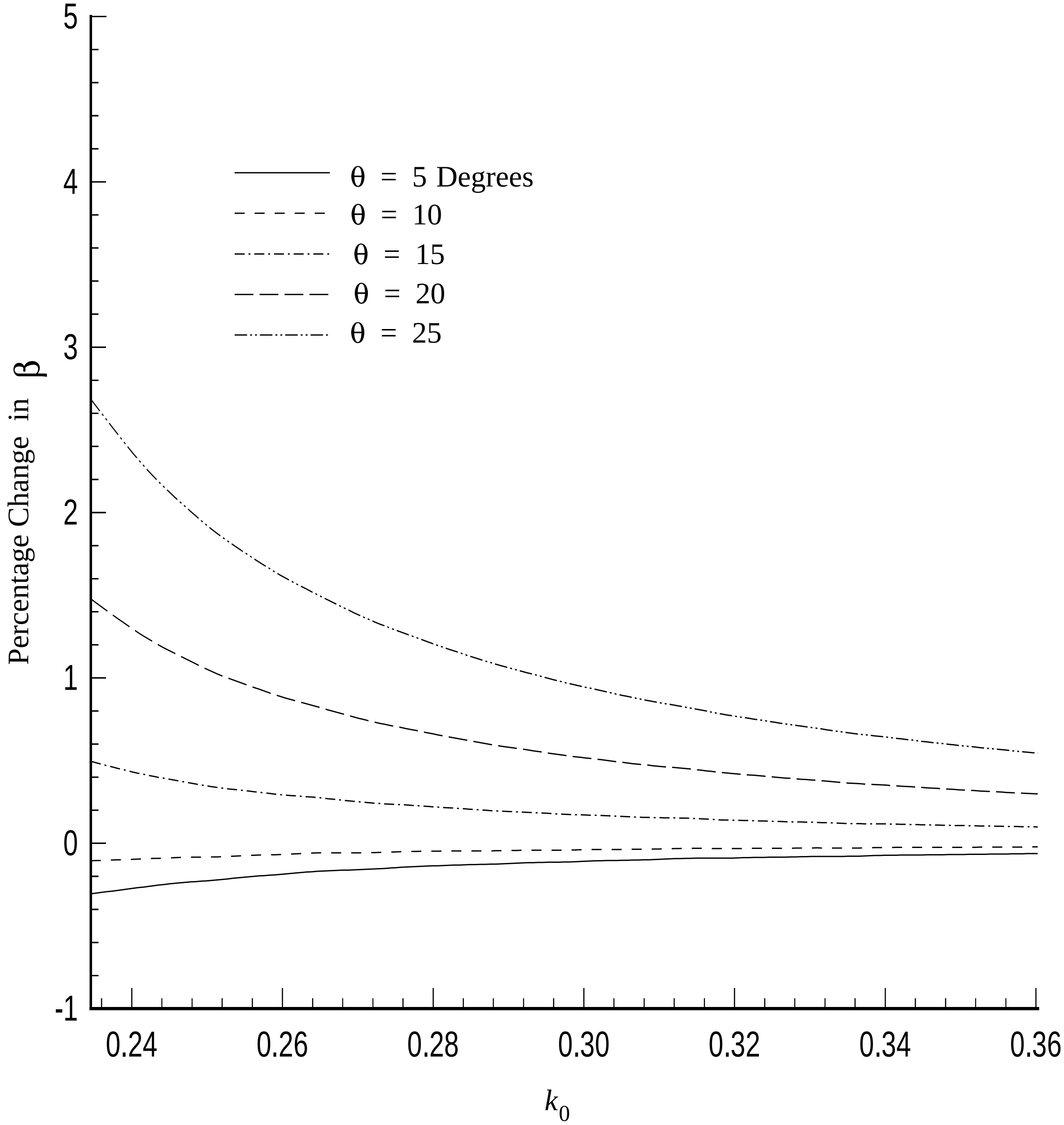

Figure 11 Plot of percentage change in dispersion characteristics of L-band rectangular waveguide for various inclination with respect to x-axis.

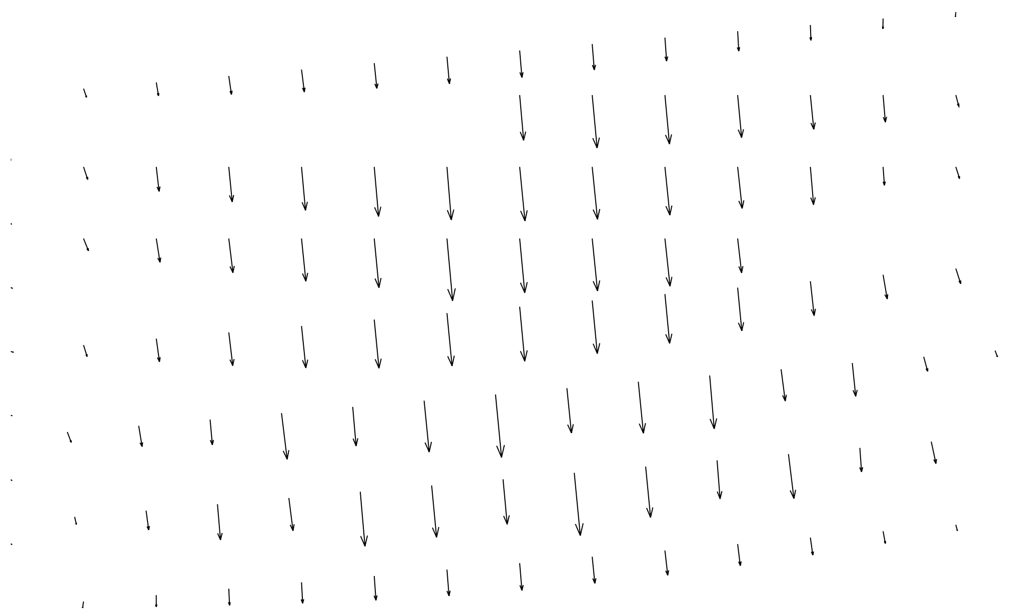

Figure 12 Electric field in the cross section of distorted L-band rectangular waveguide shown in Figure 8 (frequency = 1.4 GHz).

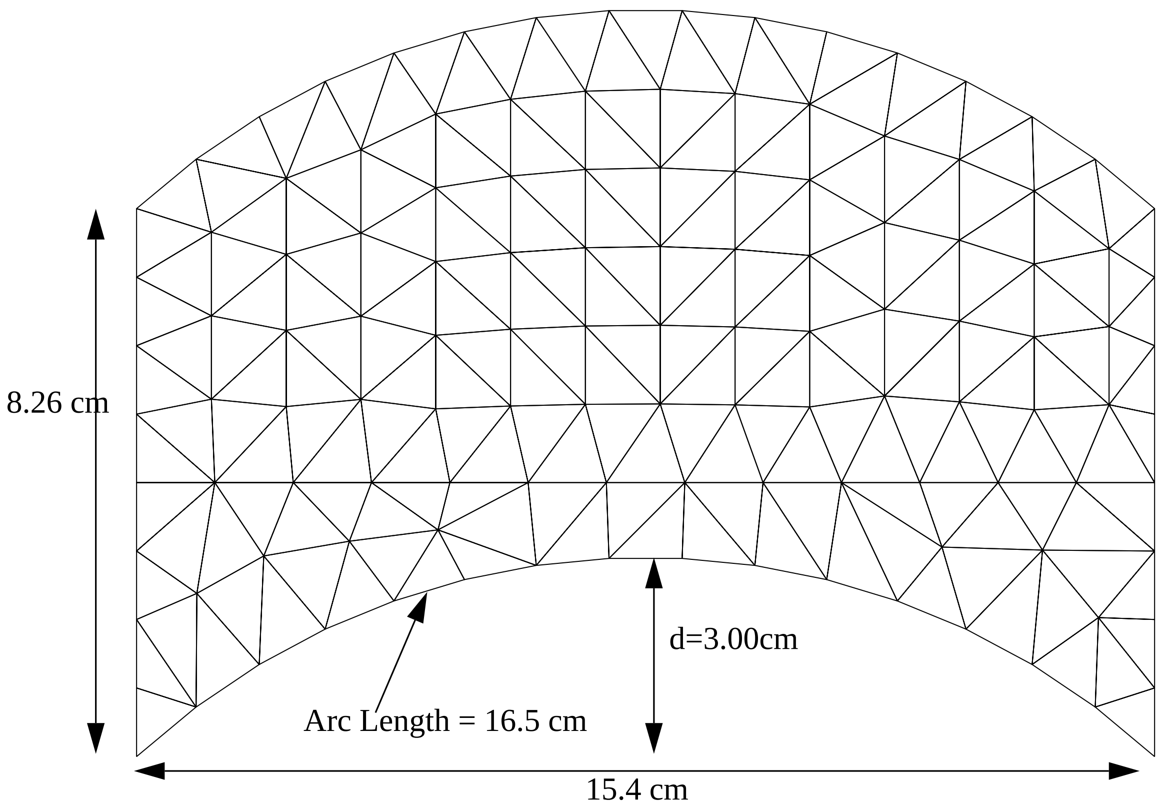

Figure 13 Geometry of L-band rectangular waveguide with distortion in x-walls.

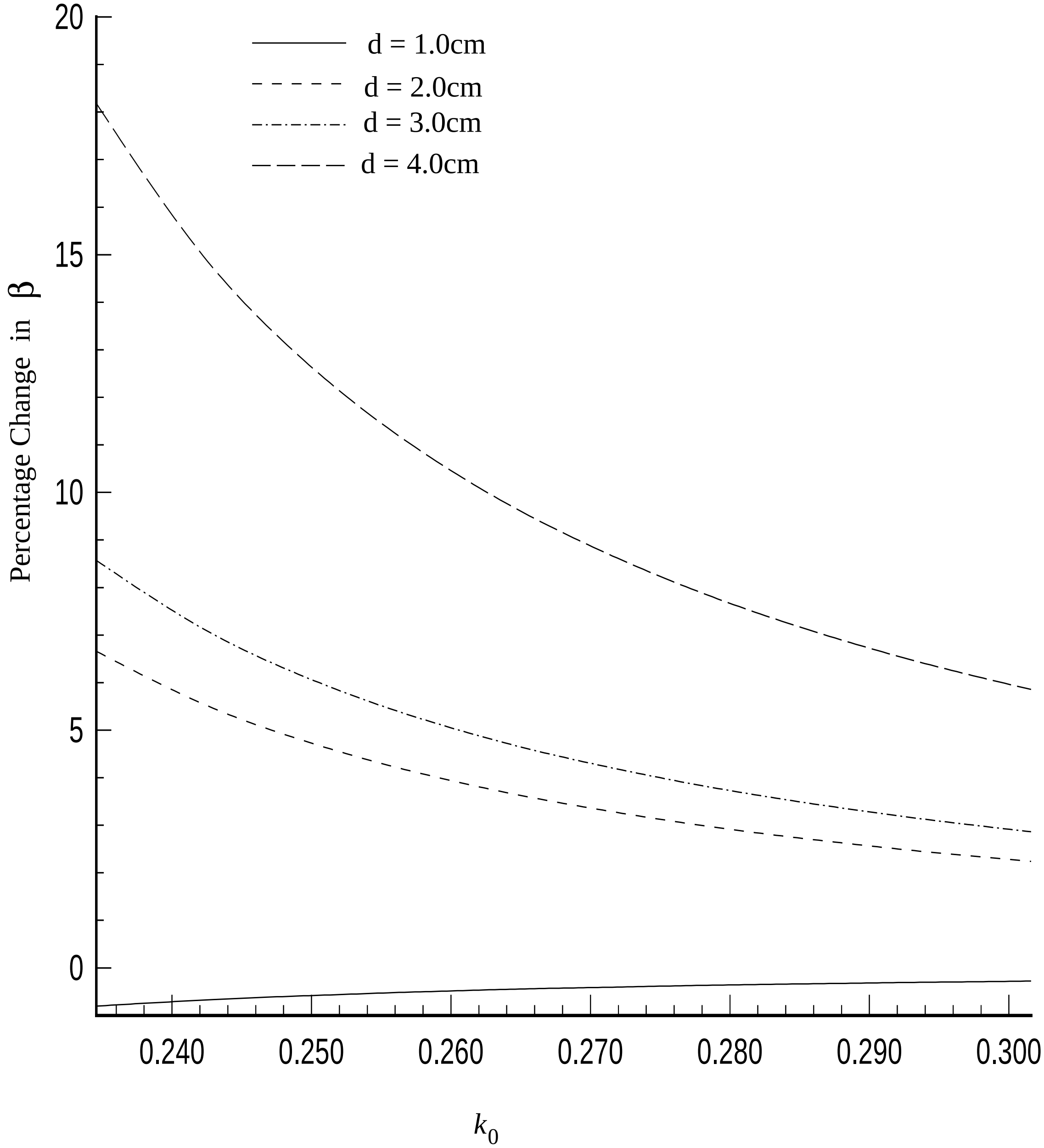

Figure 14 Plot of percentage change in dispersion characteristics of L-band rectangular waveguide with distortion as shown in Figure 13.

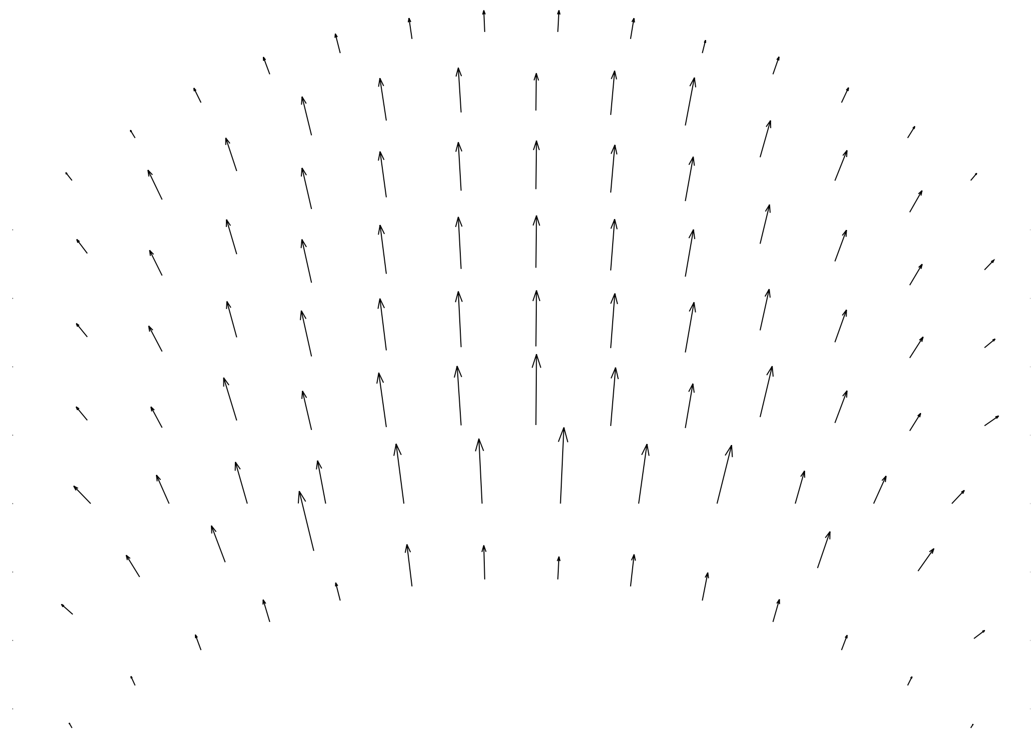

Figure 15 Electric field in the cross section of distorted L-band rectangular waveguide shown in Figure 13 (frequency = 1.4 GHz).

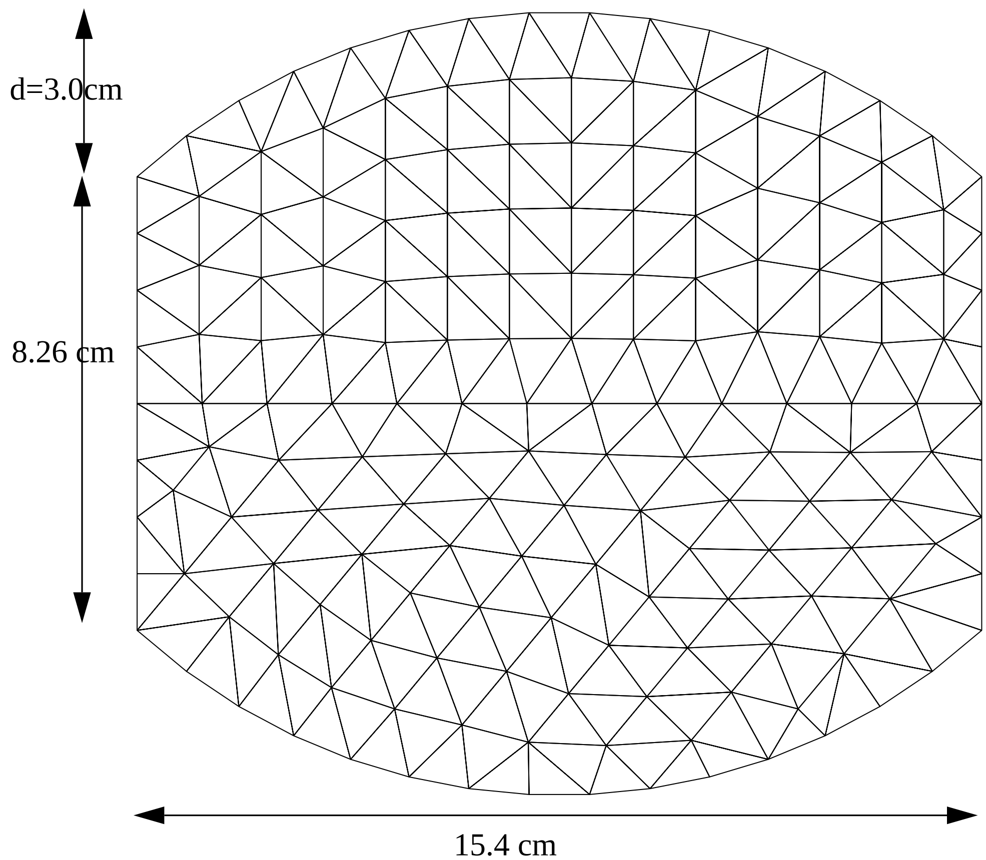

Figure 16 Geometry of L-band rectangular waveguide with distortion in x-walls.

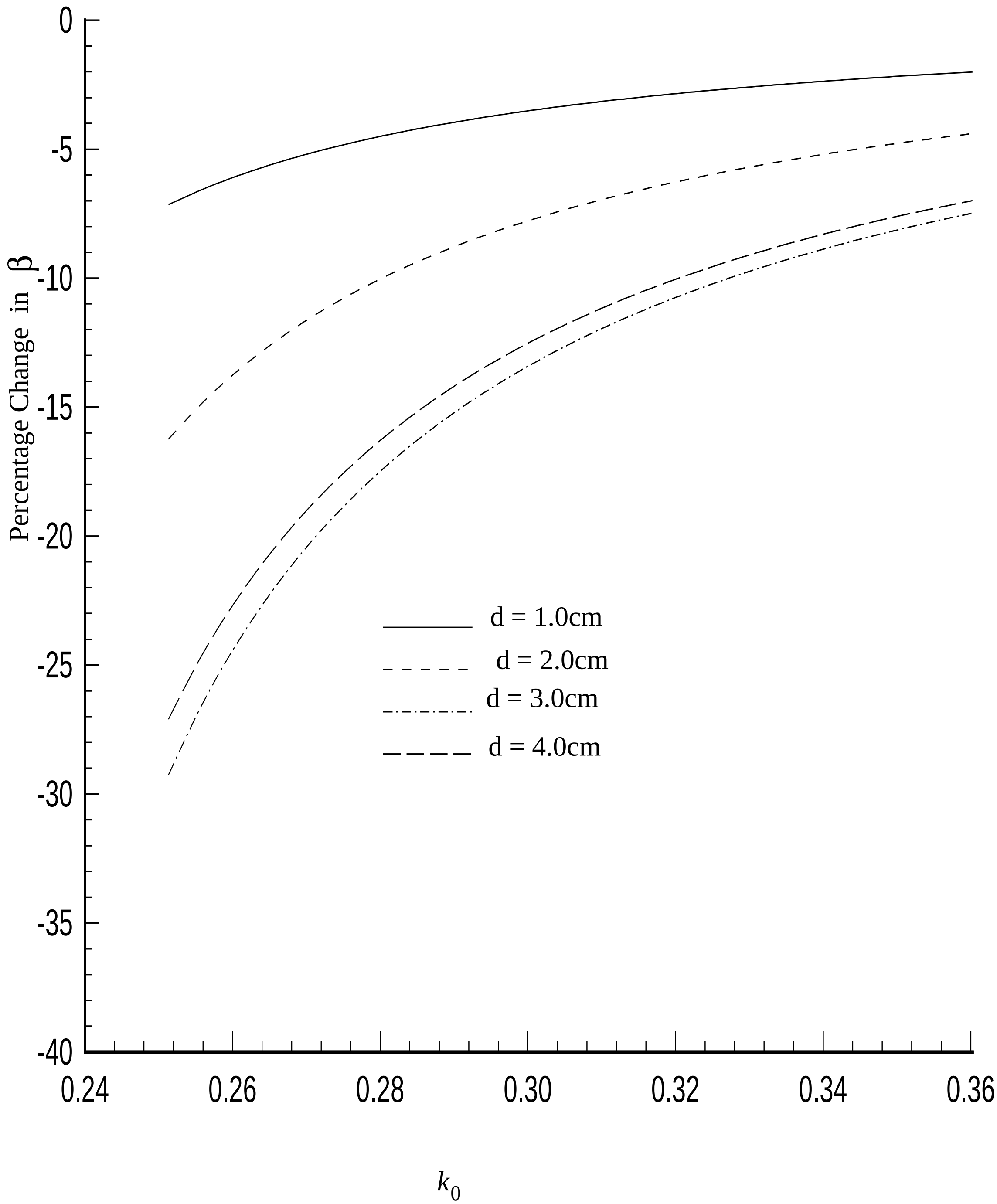

Figure 17 Plot of percentage change in dispersion characteristics of L-band rectangular waveguide with distortion as shown in Figure 16.

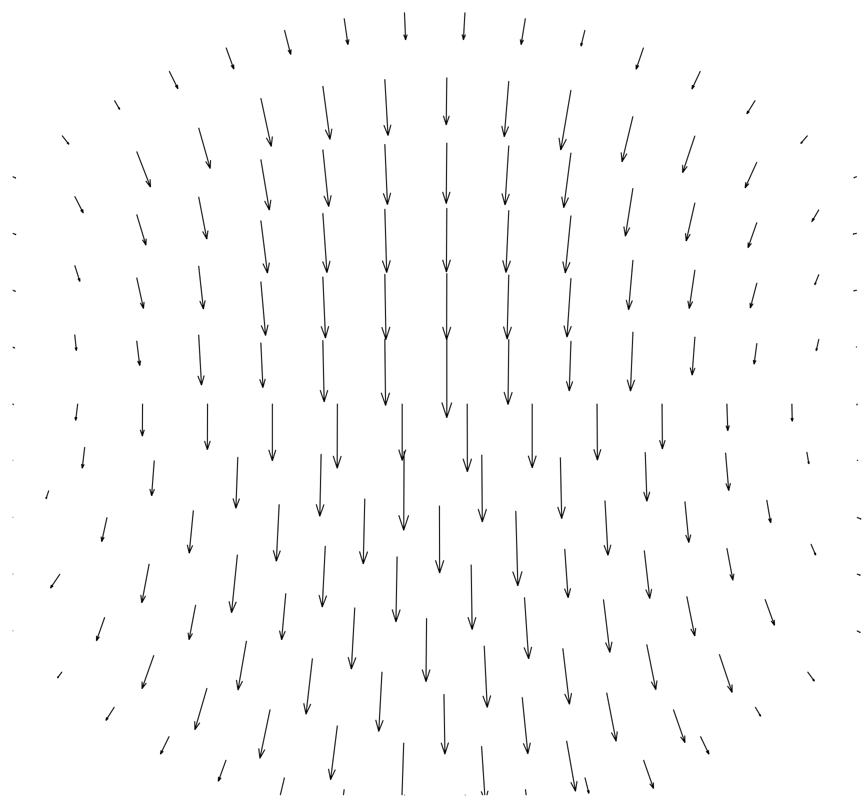

Figure 18 Electric field in the cross section of distorted L-band rectangular waveguide shown in Figure 16 (frequency = 1.4 GHz).

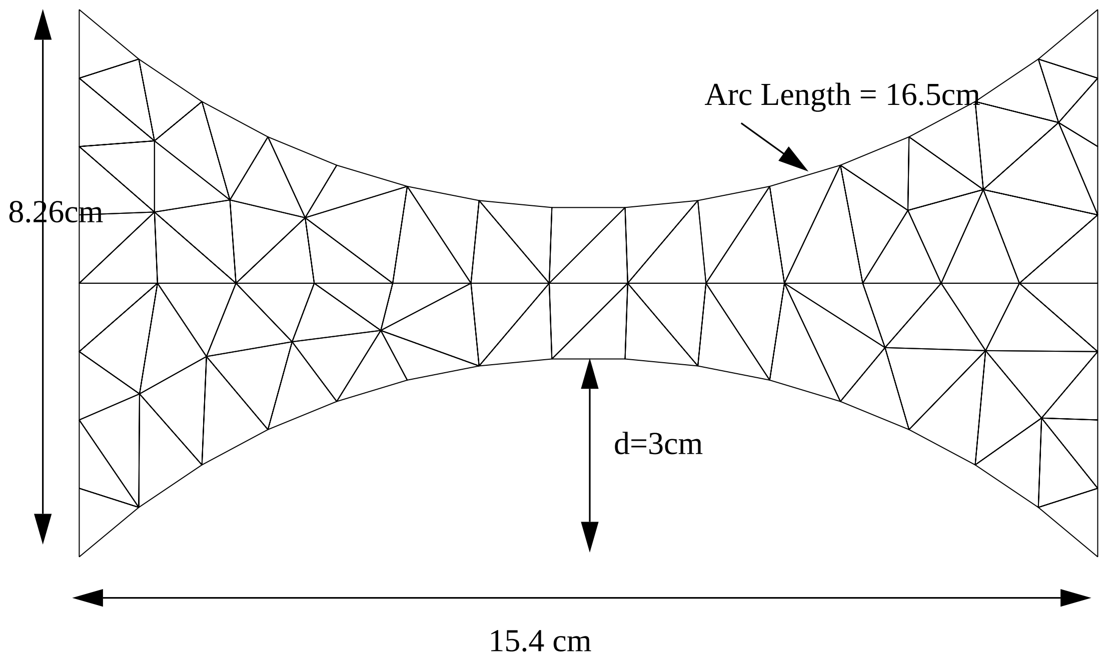

Figure 19 Geometry of L-band rectangular waveguide with distortion in x-walls.

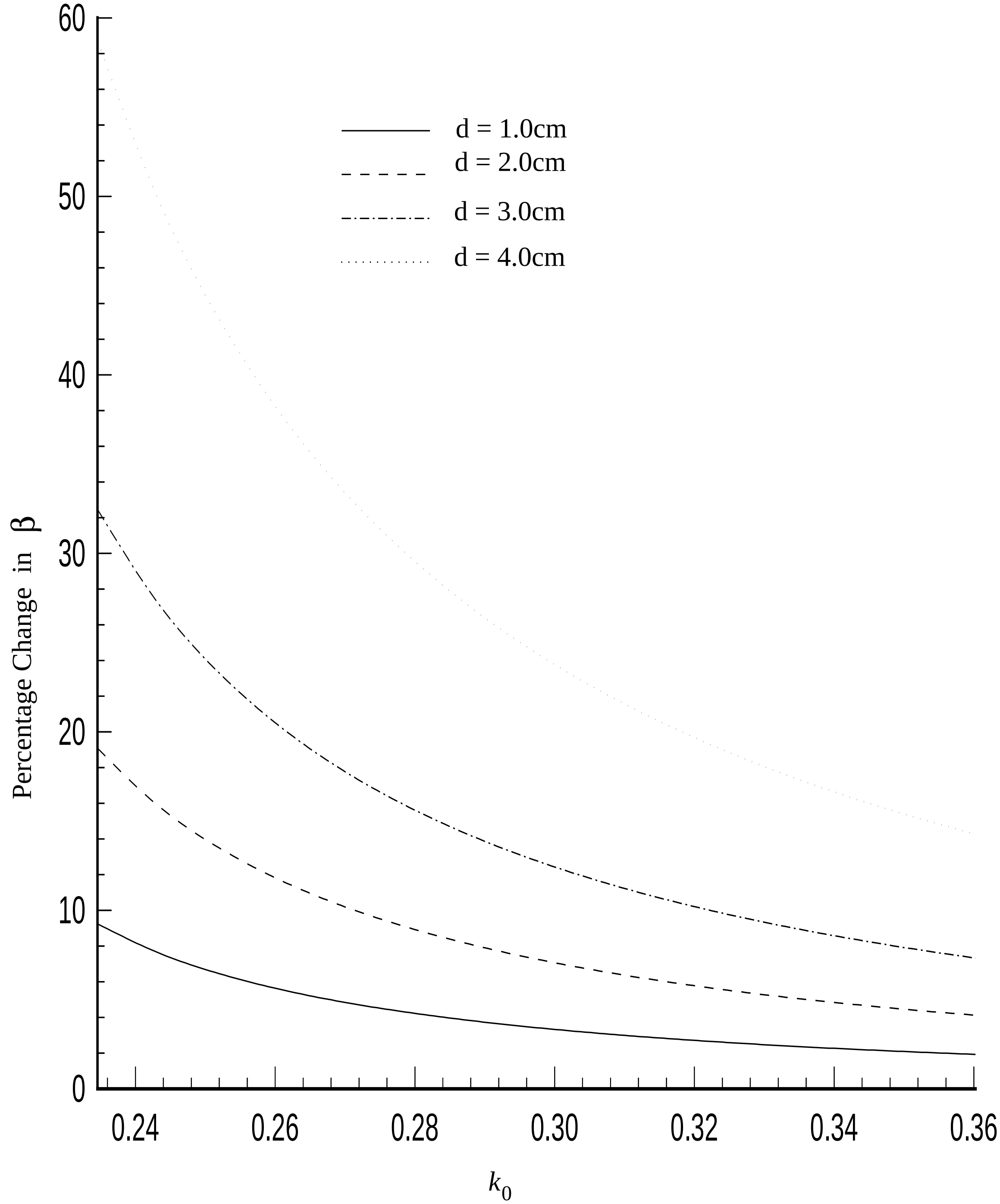

Figure 20 Plot of percentage change in dispersion characteristics of L-band rectangular waveguide with distortion as shown in Figure 19.

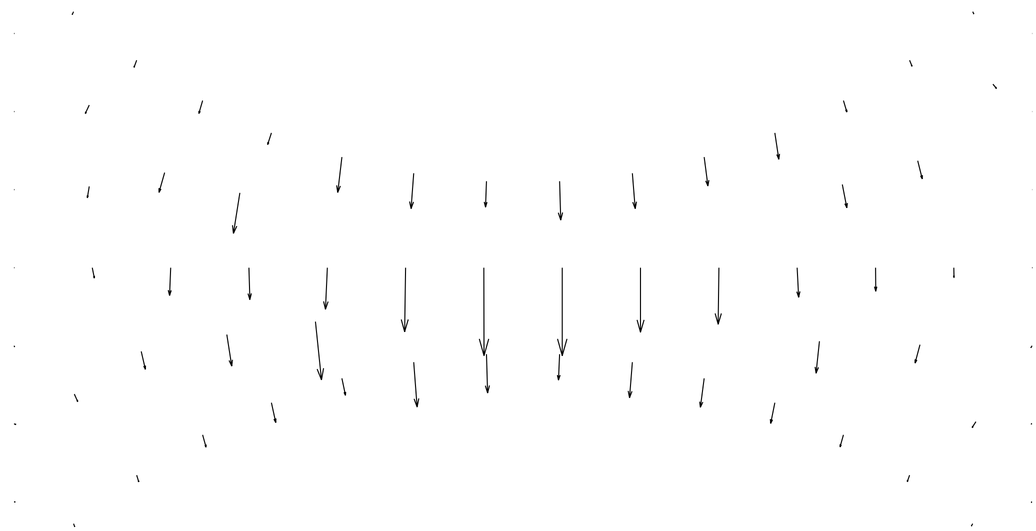

Figure 21   Electric field in the cross section of distorted L-band rectangular waveguide shown in Figure 19 (frequency = 1.4 GHz).

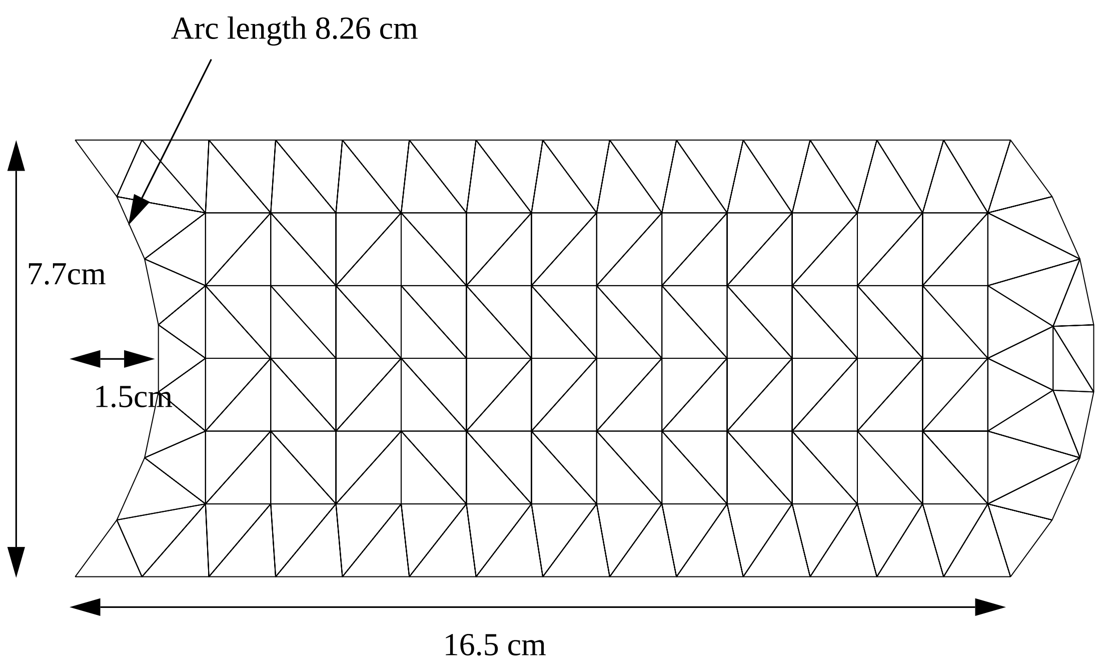

Figure 22 Geometry of L-band rectangular waveguide with distortion in y-walls.

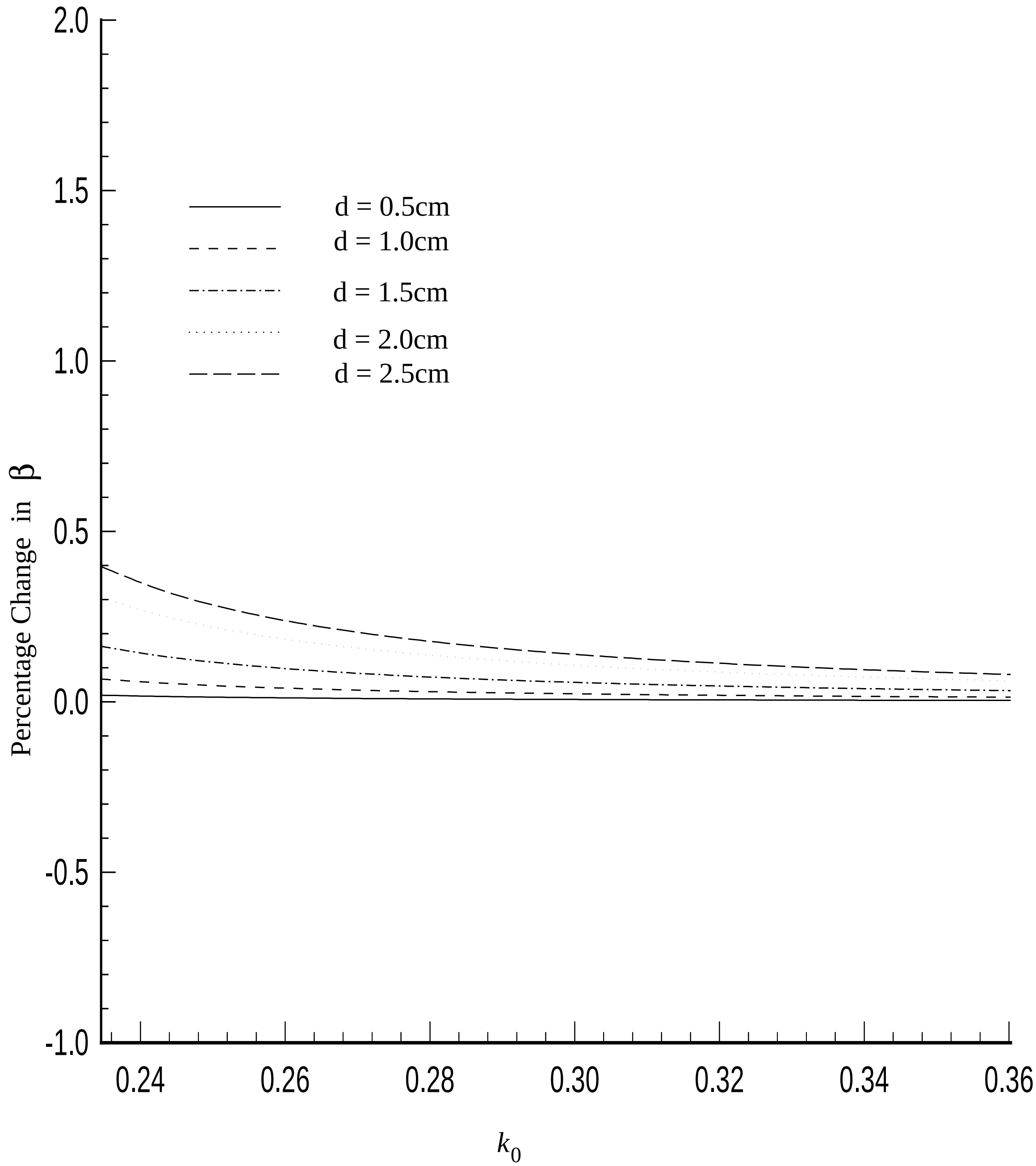

Figure 23 Plot of percentage change in dispersion characteristics of L-band rectangular waveguide with distortion as shown in Figure 22.

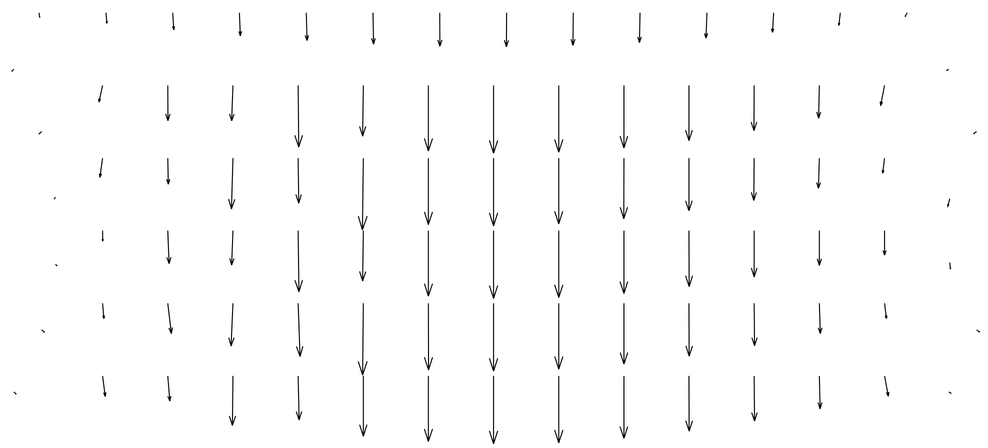

Figure 24 Electric field in the cross section of distorted L-band rectangular waveguide shown in Figure 22 (frequency = 1.4 GHz).

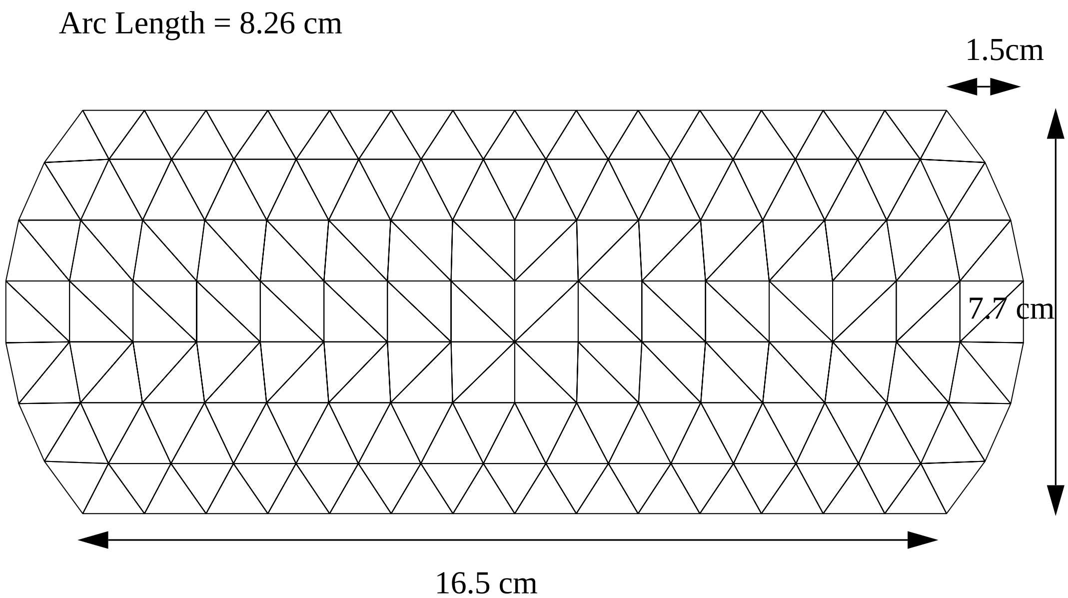

Figure 25 Geometry of L-band rectangular waveguide with distortion in y-walls.

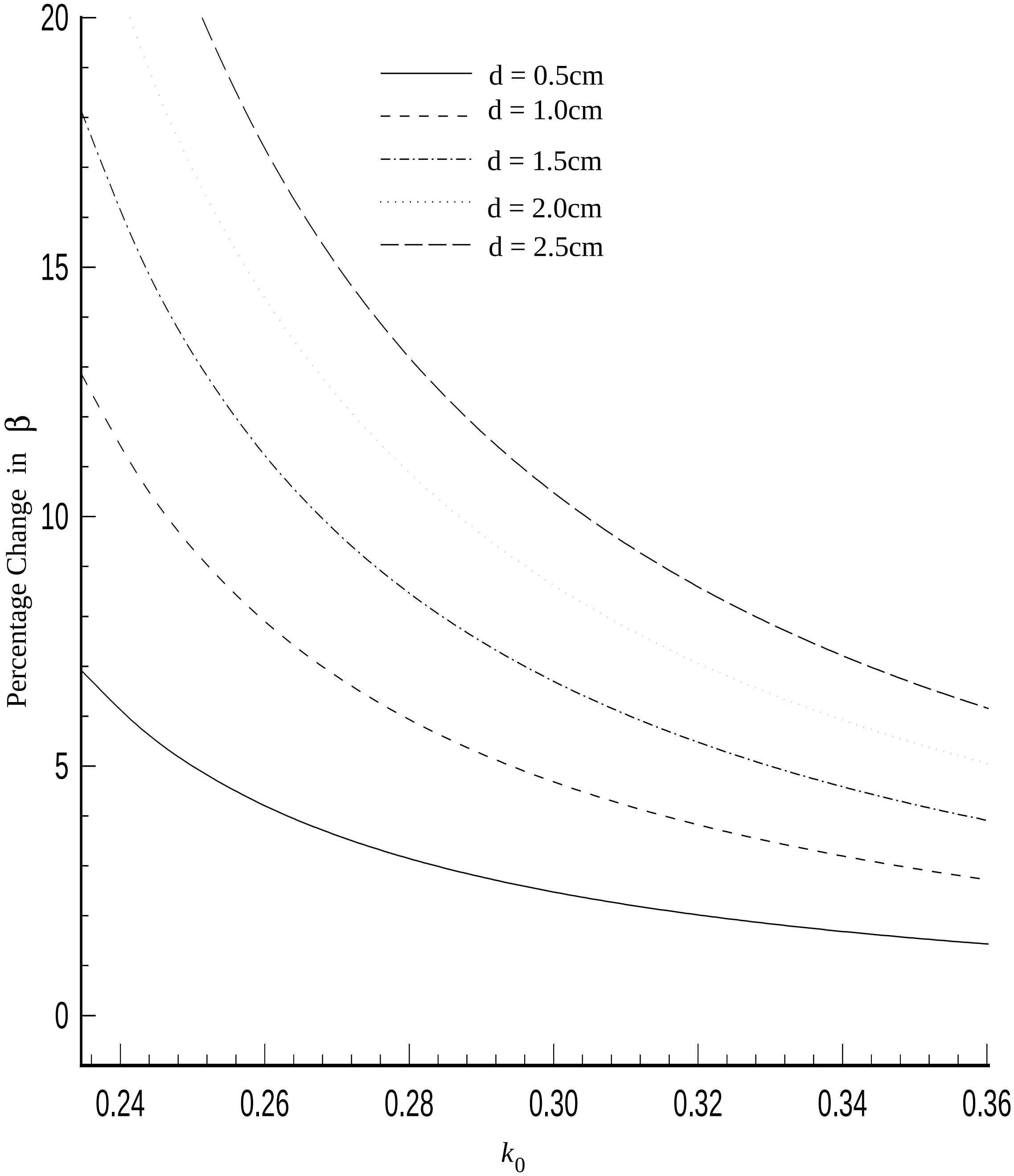

Figure 26 Plot of percentage change in dispersion characteristics of L-band rectangular waveguide with distortion as shown in Figure 25.

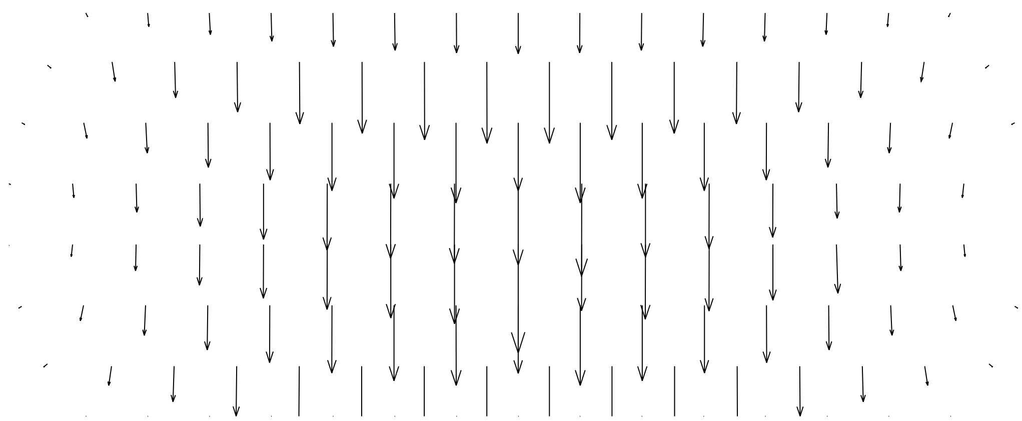

Figure 27   Electric field in the cross section of distorted L-band rectangular waveguide shown in Figure 25 (frequency = 1.4 GHz).

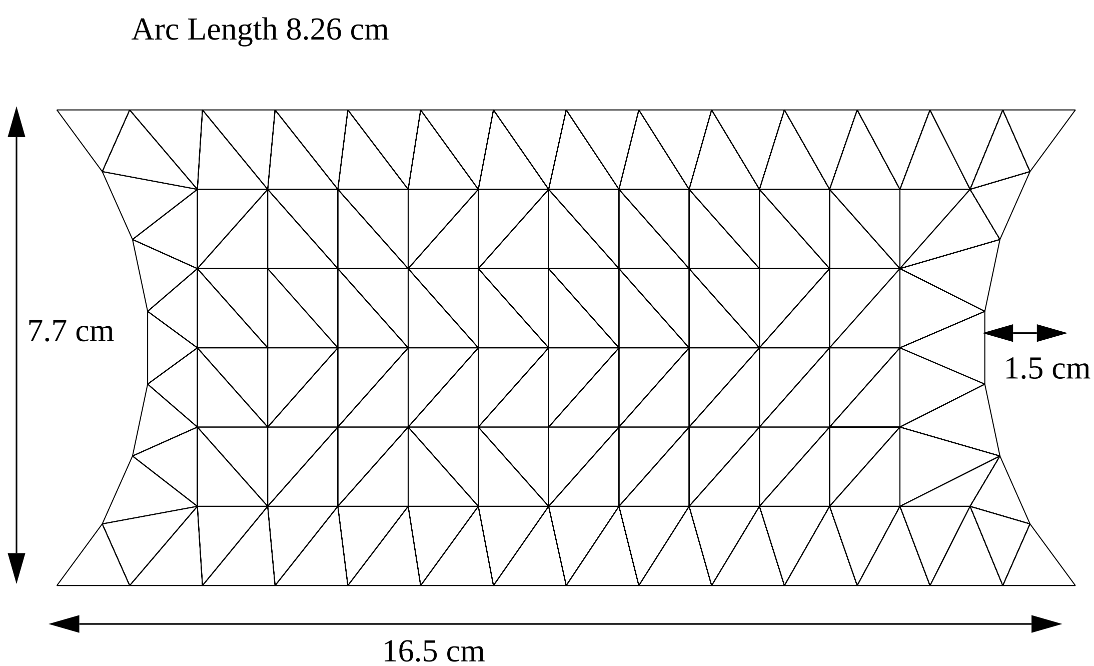

Figure 28 Geometry of L-band rectangular waveguide with distortion in y-walls.

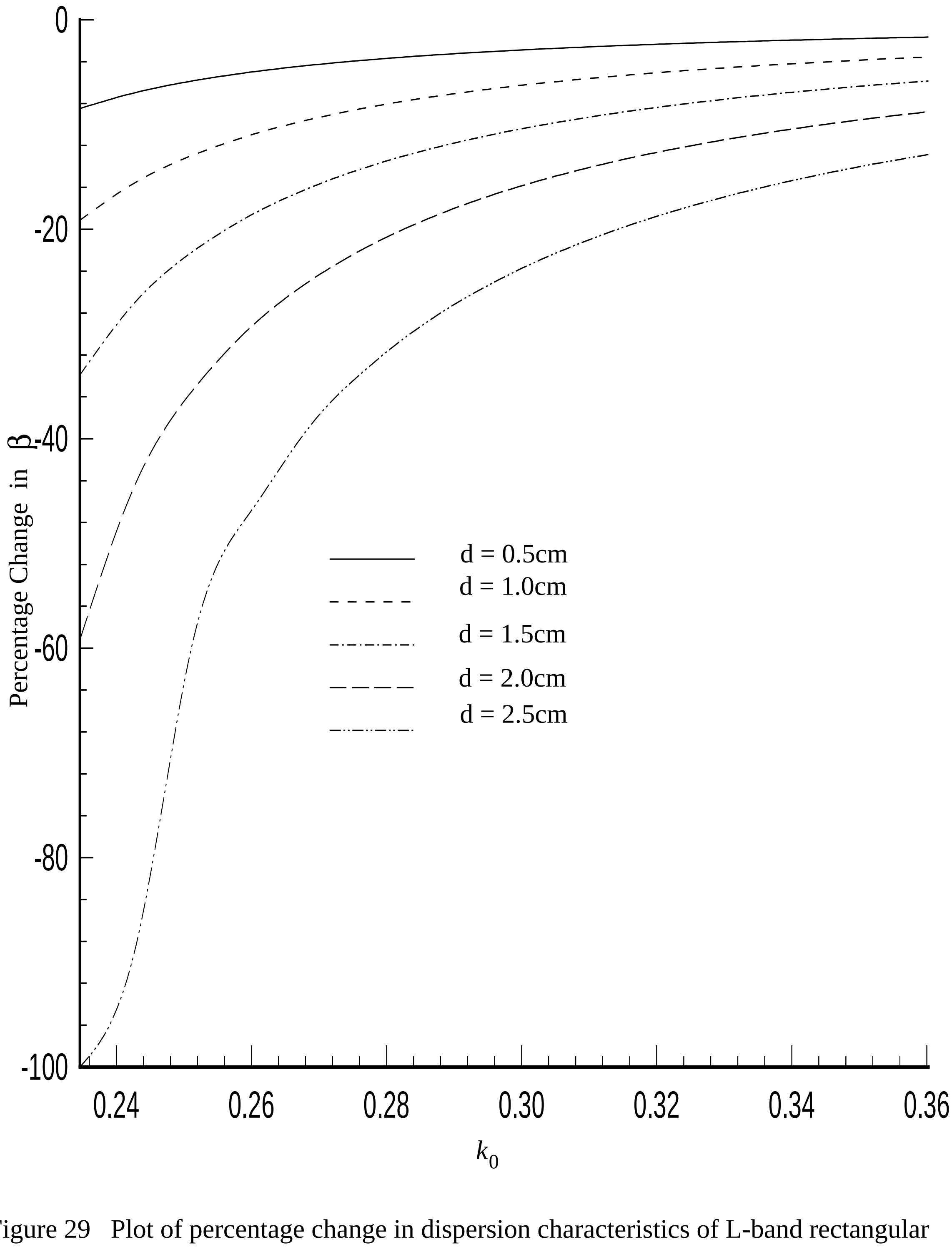

Figure 29 Plot of percentage change in dispersion characteristics of L-band rectangular waveguide with distortion as shown in Figure 28.

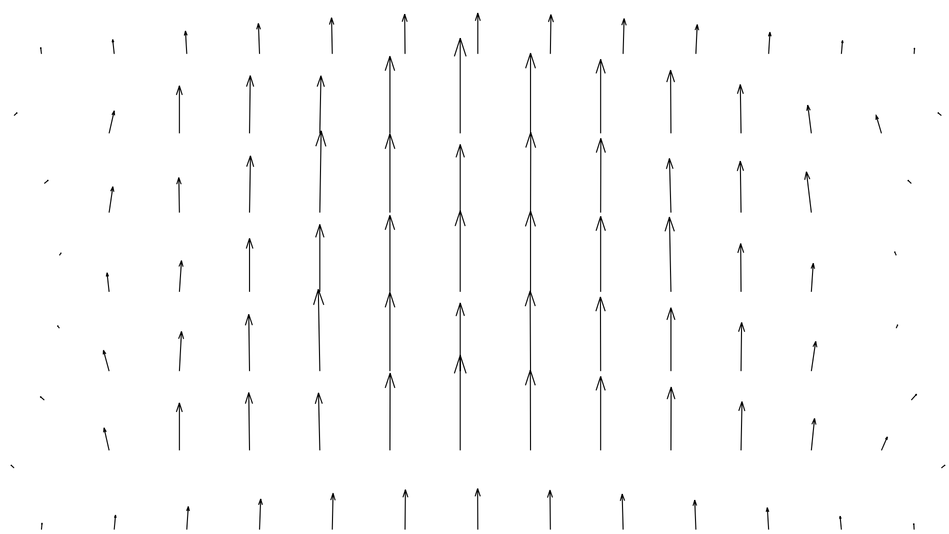

Figure 30   Electric field in the cross section of distorted L-band rectangular waveguide shown in Figure 28 (frequency = 1.4 GHz).

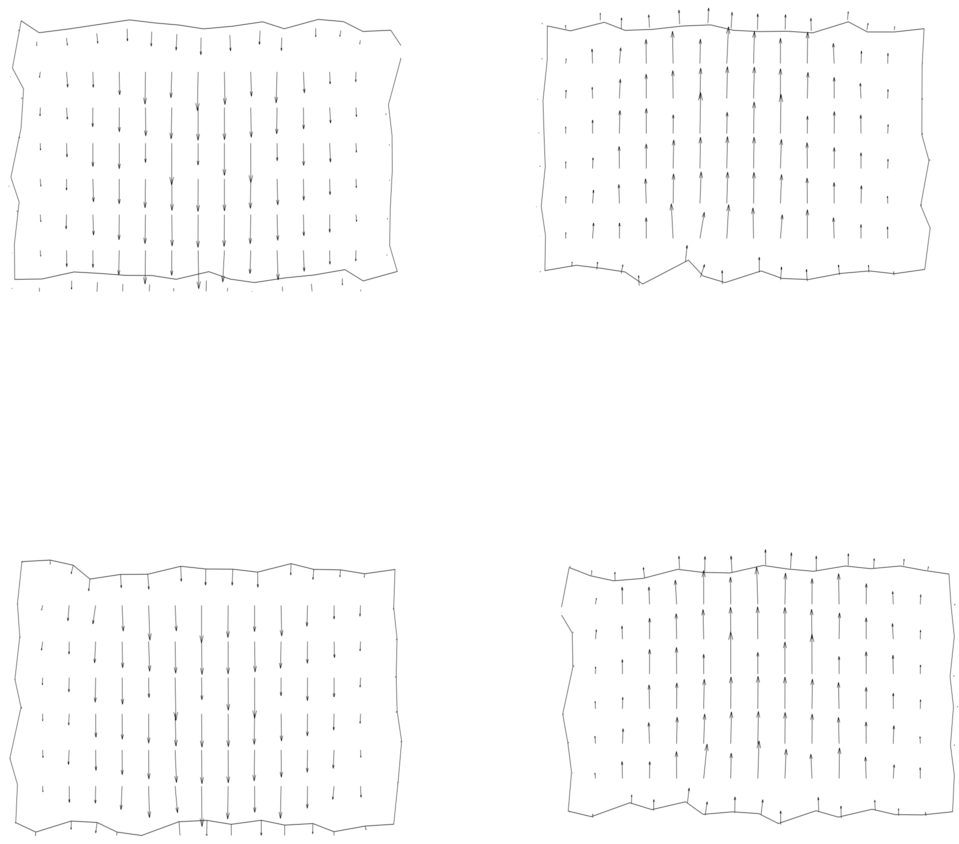

Figure 31 Geometries of rectangular waveguides with random distortion in wall boundaries ($\sigma^2 = 0.2$ and tolerance = +/-0.2)(cont.).

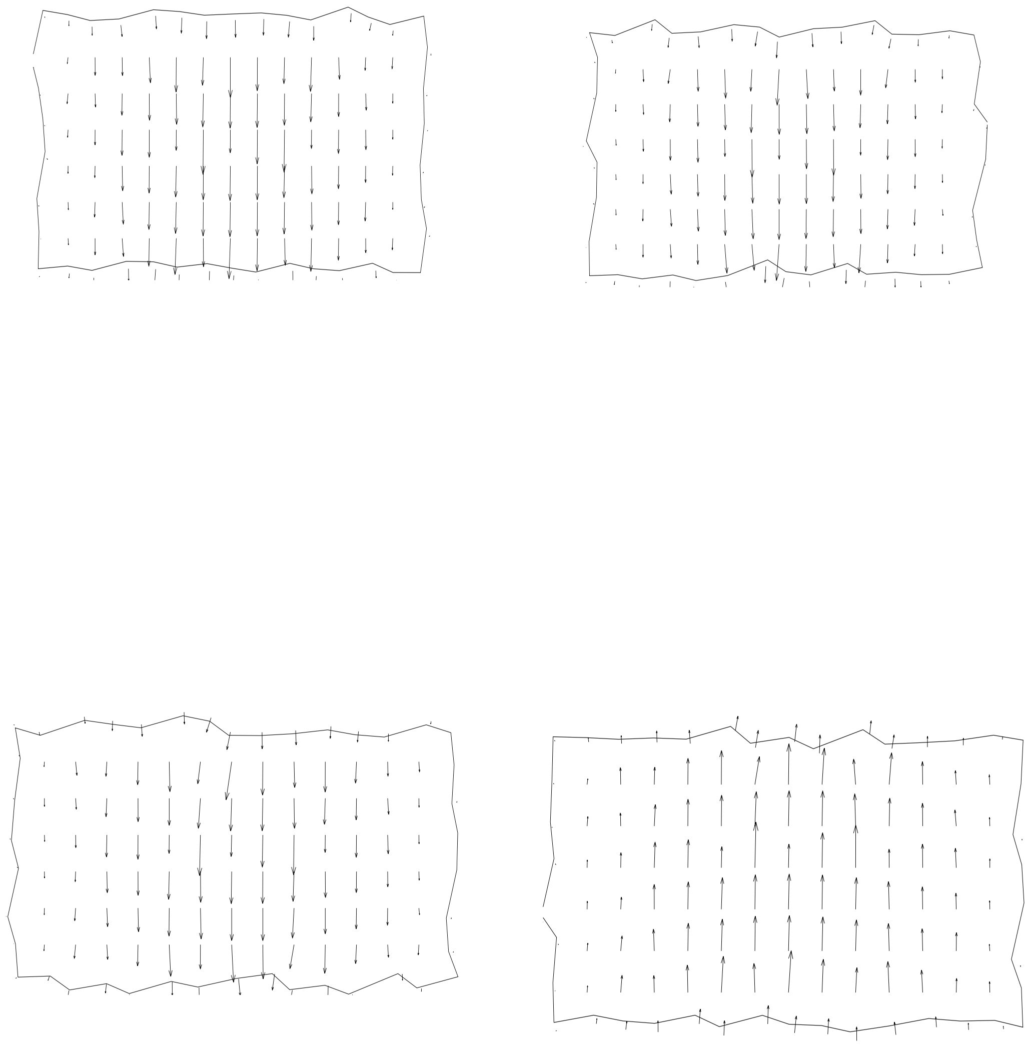

Figure 31 Geometries of rectangular waveguides with random distortion in wall boundaries ($\sigma^2 = 0.2$ and tolerance = +/-0.2) (completed).

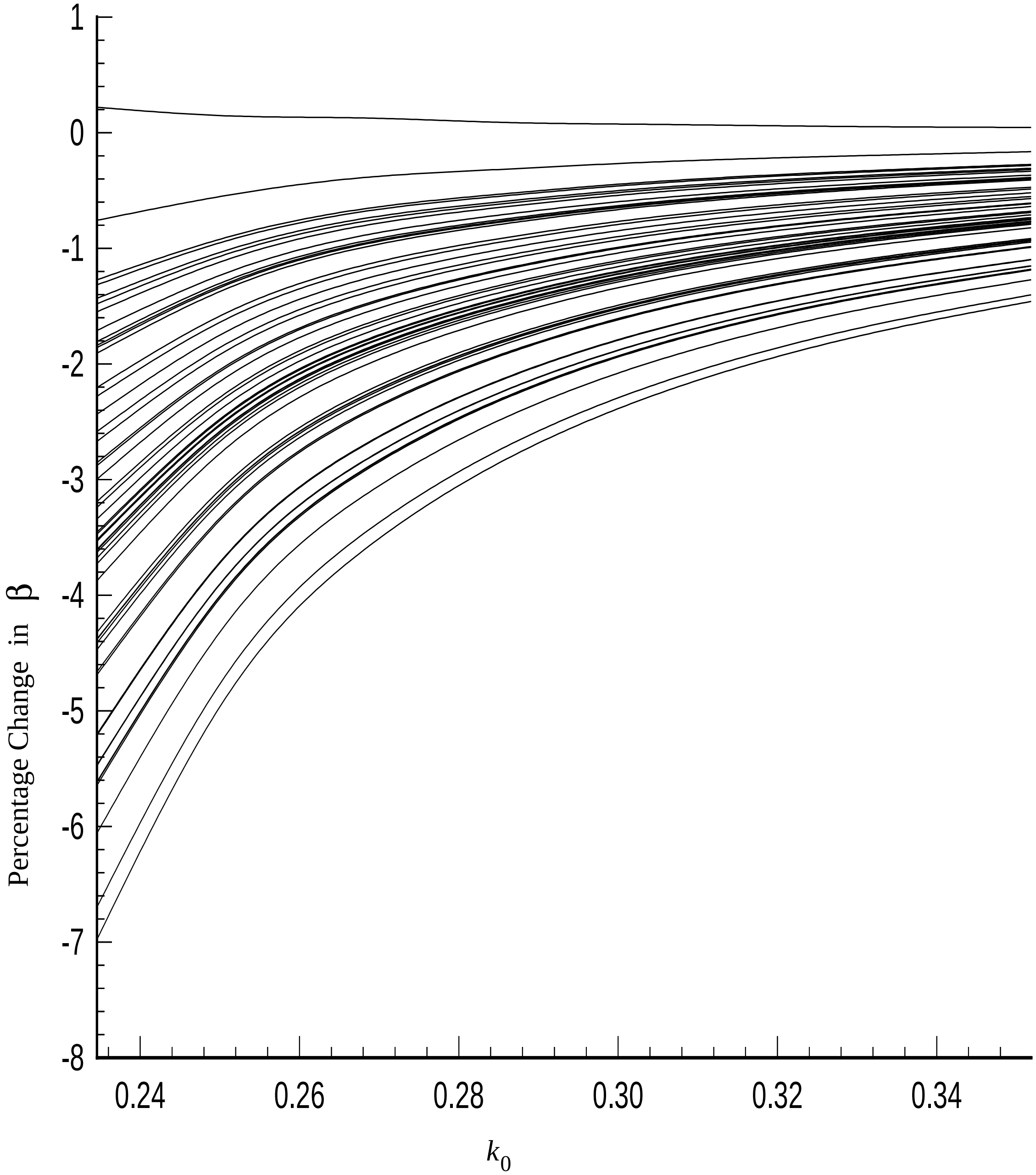

Figure 32 Plot of percentage change in dispersion characteristics of L-band rectangular waveguide for $\sigma^2 = 0.2$ and tolerance = ± 0.2.

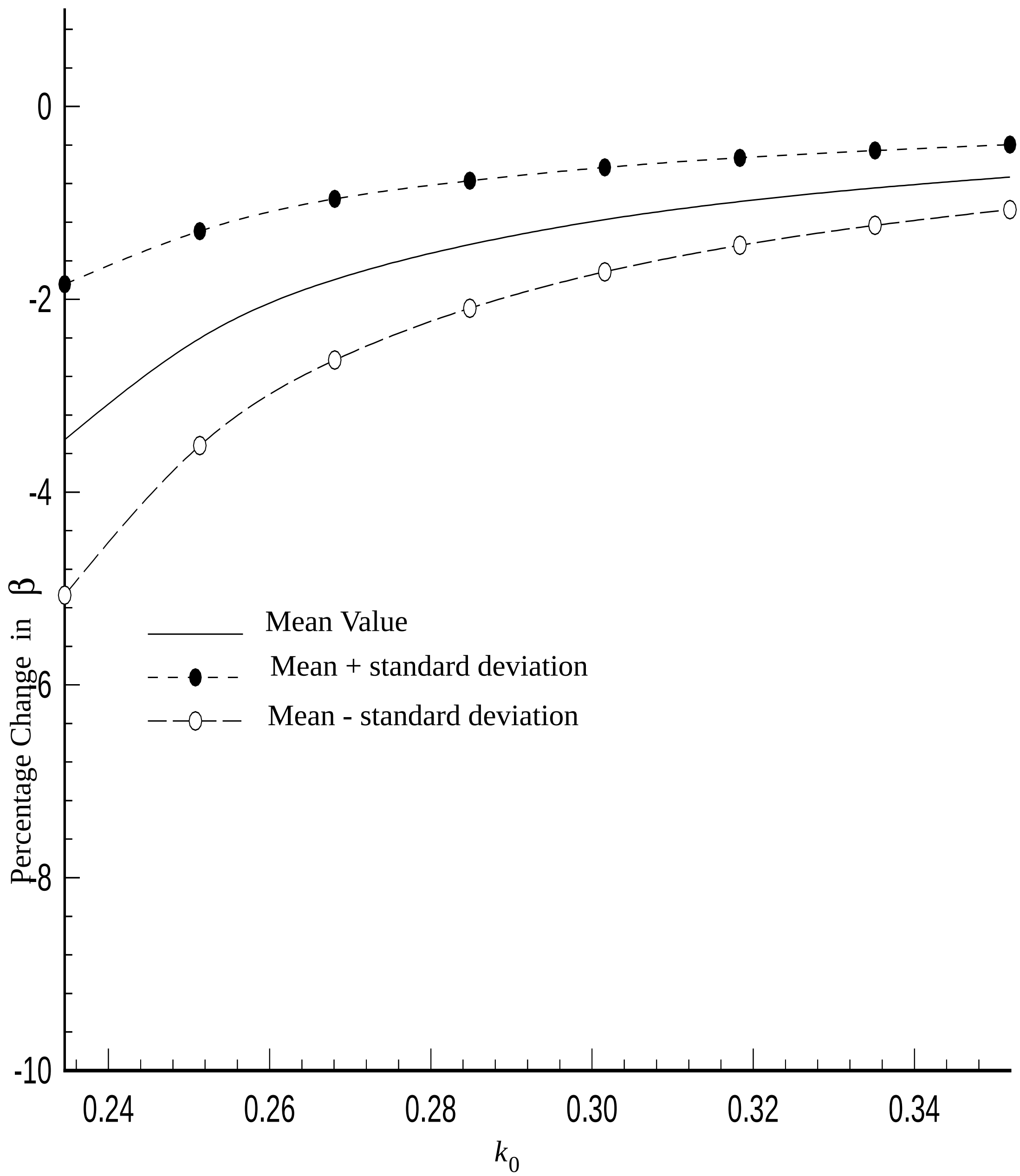

Figure 33 Plot of percentage change in dispersion characteristics of L-band rectangular waveguide, mean value, and standard deviation calculated from Figure 31.

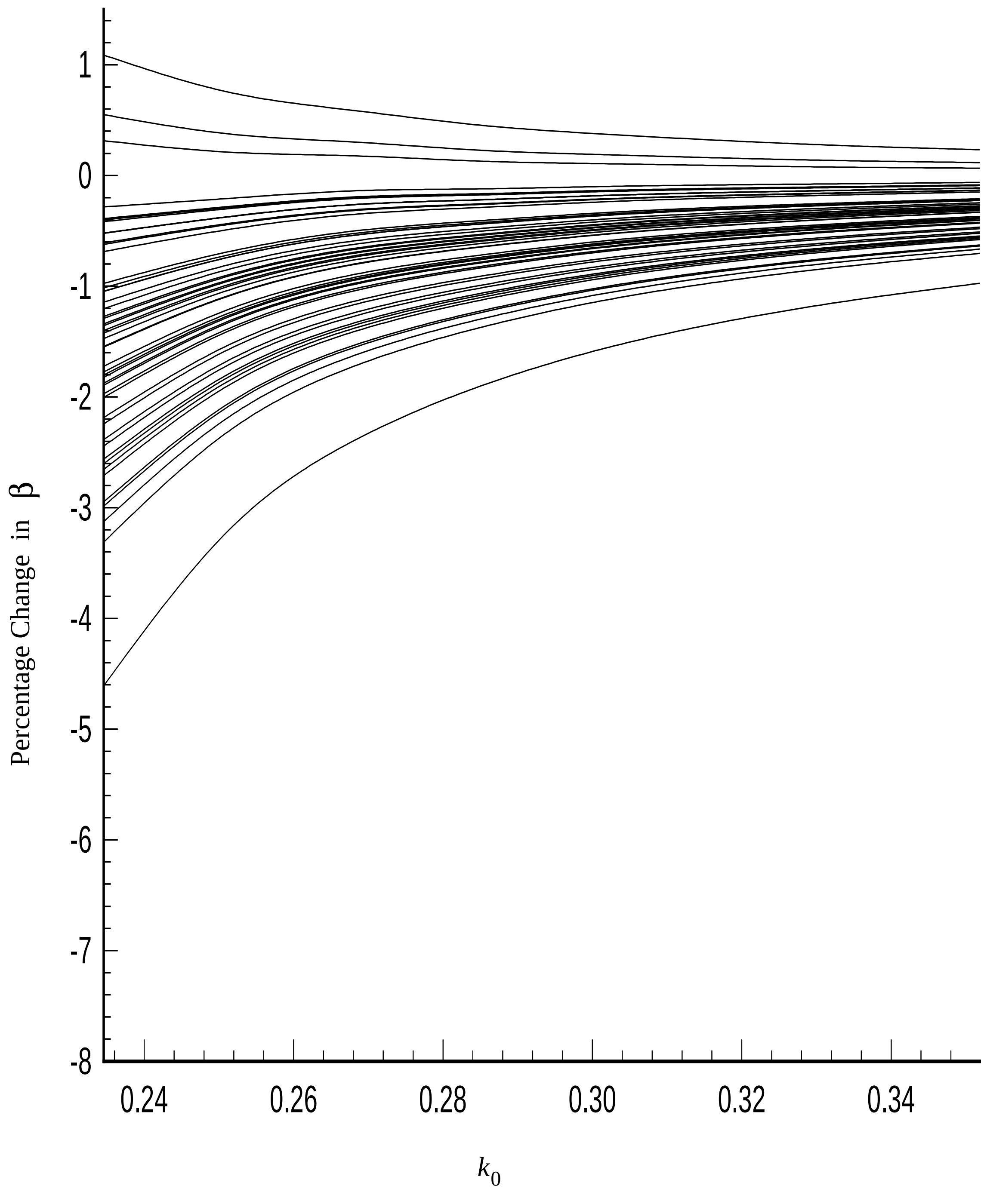

Figure 34 Plot of percentage change in dispersion characteristics of L-band rectangular waveguide for $\sigma^2 = 0.2$ and tolerance = ± 0.1.

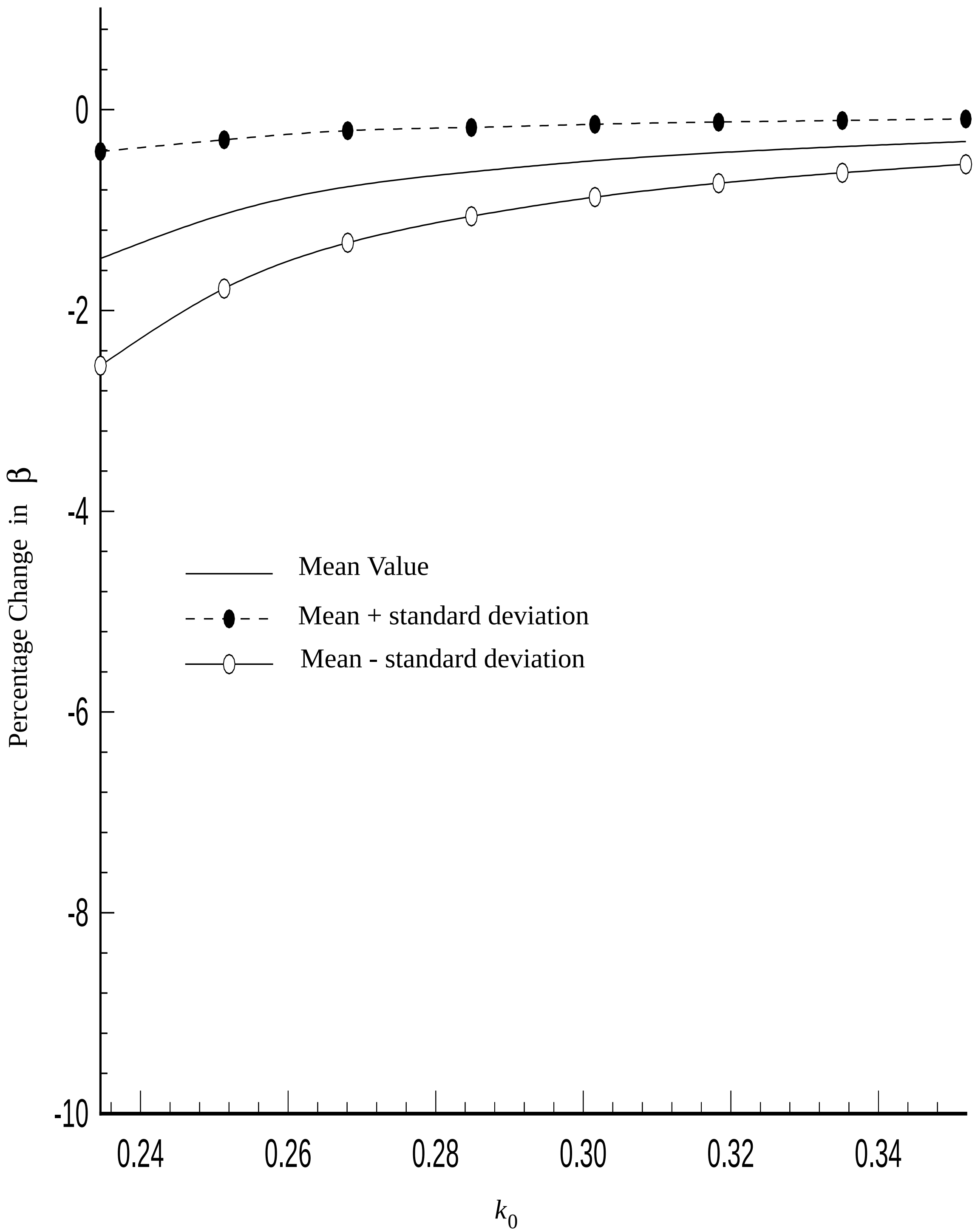

Figure 35 Plot of percentage change in dispersion characteristics of L-band rectangular waveguide, mean value, and standard deviation calculated from Figure 34.

REPORT DOCUMENTATION PAGE	Form Approved OMB No. 0704-0188

1. AGENCY USE ONLY (Leave blank)	2. REPORT DATE	3. REPORT TYPE AND DATES COVERED
	February 1998	Contractor Report

4. TITLE AND SUBTITLE
Application of Finite Element Method to Analyze Inflatable Waveguide Structures

5. FUNDING NUMBERS
NAS1-19341

522-11-41-02

6. AUTHOR(S)
M. D. Deshpande

7. PERFORMING ORGANIZATION NAME(S) AND ADDRESS(ES)
NASA Langley Research Center
Hampton, VA 23681-2199

8. PERFORMING ORGANIZATION REPORT NUMBER

9. SPONSORING/MONITORING AGENCY NAME(S) AND ADDRESS(ES)
National Aeronautics and Space Administration
Washington, DC 20546-0001

10. SPONSORING/MONITORING AGENCY REPORT NUMBER
NASA/CR-1998-206928

11. SUPPLEMENTARY NOTES
Langley Technical Monitor: M. C. Bailey

12a. DISTRIBUTION/AVAILABILITY STATEMENT
Unclassified-Unlimited
Subject Category 17 Distribution: Nonstandard
Availability: NASA CASI (301) 621-0390

12b. DISTRIBUTION CODE

13. ABSTRACT (Maximum 200 words)
A Finite Element Method (FEM) is presented to determine propagation characteristics of deformed inflatable rectangular waveguide. Various deformations that might be present in an inflatable waveguide are analyzed using the FEM. The FEM procedure and the code developed here are so general that they can be used for any other deformations that are not considered in this report. The code is validated by applying the present code to rectangular waveguide without any deformations and comparing the numerical results with earlier published results. The effect of the deformation in an inflatable waveguide on the radiation pattern of linear rectangular slot array is also studied.

14. SUBJECT TERMS
Inflatable Waveguides, Finite Element Method, Waveguide Discontinuity

15. NUMBER OF PAGES
62

16. PRICE CODE
A04

17. SECURITY CLASSIFICATION OF REPORT	18. SECURITY CLASSIFICATION OF THIS PAGE	19. SECURITY CLASSIFICATION OF ABSTRACT	20. LIMITATION OF ABSTRACT
Unclassified	Unclassified	Unclassified	